Hillslopes in Headwaters of Qinghai-Tibetan Plateau as Hotspots for Subsurface Dissolved Organic Carbon Processing during Permafrost Thaw

Yuqin Sun[1,1], Kale Clauson[2,2], Min Zhou[1,1], Ziyong Sun[3,3], Chunmiao Zheng[4,4], and Yan Zheng[4,4]

[1]Peking University
[2]Queens College, City University of New York
[3]China University of Geosciences
[4]Southern University of Science and Technology

January 20, 2023

Abstract

Climate warming has accelerated thawing of northern permafrost, resulting in changes to the supply of dissolved organic carbon (DOC) to inland waters with uncertain fate. Extensive surface – groundwater interactions occur in alpine permafrost watersheds and likely influence DOC processing differently than systems with limited interactions. Here, we quantify and characterize DOC in waters collected from eight water types sampled across a small (25 km2) alpine (elevation 2960 to 4820 m a.s.l) watershed in the Qinghai-Tibetan Plateau (QTP) containing variably degraded permafrost. Three types of water (thermokarst ponds, red mud gully and seepage-I) contained high DOC concentrations (5.2 to 22.6 mg/L, n=38), with C contributions predominantly from frozen soil meltwater. Spatial patterns of DOC in stream (0.3 to 4.8 mg L-1, n=41), and subsurface waters (0.4 to 3.8 mg/L, n=34), all contained frozen soil meltwater C as constrained by δ18O and electrical conductivity, reflecting surface – groundwater exchanges in the upper-, mid- and lower stretches of the watershed. Further, patterns of increasing DOC loss (ΔDOC) in subsurface waters with decreased proportions of protein-like organic matter and SUVA254, suggest subsurface microbial processing. Using previously established biodegradation DOC kinetics (0.06 d-1) from the QTP, the groundwater transit time is estimated to be between 6 and 20 days based on ΔDOC changes of 32% and 74% for July and September, respectively. Mass balance of DOC inputs and export fluxes demonstrate nearly half of all DOC was lost in this small watershed, indicating hillslopes are hotspots for DOC processing, with subsurface environments playing a key role.

Hillslopes in Headwaters of Qinghai-Tibetan Plateau as Hotspots for Subsurface Dissolved Organic Carbon Processing during Permafrost Thaw

Yuqin Sun[1,2,3], Kale Clauson[4], Min Zhou[1], Ziyong Sun[5], Chunmiao Zheng[2,3] and Yan Zheng[2,3*]

[1] College of Engineering, Peking University, Beijing, 100871, China.

[2] State Environmental Protection Key Laboratory of Integrated Surface Water-Groundwater Pollution Control, School of Environmental Science and Engineering, Southern University of Science and Technology, Shenzhen, 518055, China.

[3] Guangdong Provincial Key Laboratory of Soil and Groundwater Pollution Control, School of Environmental Science and Engineering, Southern University of Science and Technology, Shenzhen, 518055, China.

[4] School of Earth and Environmental Sciences, Queens College, City University of New York, Flushing, NY 11367, USA.

[5] School of Environmental Studies, China University of Geosciences, Wuhan, 430074, China.

Corresponding author: Yan Zheng (yan.zheng@sustech.edu.cn) ORCID 0000-0001-5256-9395

Key Points

- Surface and subsurface waters in an alpine watershed of Qinghai-Tibetan Plateau contain permafrost sourced bioavailable DOC.
- Hillslopes in headwaters of QTP are hotspots for subsurface DOC processing before it reaches the main river during seasonal thaw.
- New constraint is placed on hillslope groundwater mean transit time (~6 to 20 days) from the DOC loss and the biodegradation kinetics.

Abstract

Climate warming has accelerated thawing of northern permafrost, resulting in changes to the supply of dissolved organic carbon (DOC) to inland waters with uncertain fate. Extensive surface – groundwater interactions occur in alpine permafrost watersheds and likely influence DOC processing differently than systems with limited interactions. Here, we quantify and characterize DOC in waters collected from eight water types sampled across a small (25 km^2) alpine (elevation 2960 to 4820 m a.s.l) watershed in the Qinghai-Tibetan Plateau (QTP) containing variably degraded permafrost. Three types of water (thermokarst ponds, red mud gully and seepage-I) contained high DOC concentrations (5.2 to 22.6 mg/L, n=38), with C contributions predominantly from frozen soil meltwater. Spatial patterns of DOC in stream (0.3 to 4.8 mg L^{-1}, n=41), and subsurface waters (0.4 to 3.8 mg/L, n=34), all contained frozen soil meltwater C as constrained by $\delta^{18}O$ and electrical conductivity, reflecting surface – groundwater exchanges in the upper-, mid- and lower stretches of the watershed. Further, patterns of increasing DOC loss (ΔDOC) in subsurface waters with decreased proportions of protein-like organic matter and $SUVA_{254}$, suggest subsurface microbial processing. Using previously established biodegradation DOC kinetics (0.06 d^{-1}) from the QTP, the groundwater transit time is estimated to be between 6 and 20 days based on ΔDOC changes of 32% and 74% for July and September, respectively. Mass balance of DOC inputs and export fluxes demonstrate nearly half of all DOC was lost in this small watershed, indicating hillslopes are hotspots for DOC processing, with subsurface environments playing a key role.

Plain Language Summary

Climate warming leads to thawing of the northern permafrost that has increased the release of organic carbon, previously regarded as “stable”, into streams and rivers. Recent laboratory studies of Arctic permafrost show the rapid biodegradation of permafrost-derived organic carbon, but is it true? For this, we turn to a small, alpine watershed in the Qinghai-Tibetan Plateau with a gradient of permafrost degradation. First, we provide rare field evidence for widespread permafrost sourced organic carbon in a variety of water types based upon its optical properties. Secondly, we use stable isotopes and electrical conductivity as “conservative” tracers to compare with dissolved organic carbon that are “reactive” to estimate the loss of organic carbon from its

upgradient source to the downslope sampling location. The extent of the loss of DOC in subsurface environment is dependent on the travel time of the groundwater along the hillslope. The DOC originating from permafrost soil is quickly dispersed in the watershed, shedding light on previously poorly constrained surface water – groundwater interaction in such settings. Finally, a mass budget finds a large loss of organic carbon within the watershed. Therefore, hillslopes act as hotspots for permafrost-derived organic carbon processing.

Keywords

Qinghai-Tibetan Plateau, Dissolved organic carbon, Permafrost, Alpine watershed, Groundwater transit time, Fluorescence spectroscopy

1 Introduction

Northern permafrost, including 42% of the areal extent of Qinghai-Tibetan Plateau (QTP), is estimated to account for >20% of total global soil organic carbon (SOC) pool of 1832 $\times 10^{12}$ kg [*Tarnocai et al.*, 2009; *Wang et al.*, 2020]. Models assessing biogeochemical cycles of soil C have raised the concern that thaw and degradation may reverse northern permafrost regions from a current C sink to a net source, under future warming trajectories [*McGuire et al.*, 2018; *Turetsky et al.*, 2020; *Wang et al.*, 2020]. Thawed permafrost SOC enters pore waters as dissolved organic carbon (DOC), a proportion of which is exported to aquatic systems to become components of in-stream carbon cycling. About 15% of permafrost SOC may enter aquatic systems over the next 300 years under future warming scenarios [*McGuire et al.*, 2018]. In the high latitude Arctic permafrost region, CO_2 evasion from inland waters is estimated to account for between 40×10^9 to 84×10^9 kg C yr^{-1} [*McGuire et al.*, 2009], but little is known about CO_2 evasion from inland waters in high altitude permafrost regions such as the QTP.

Streams and rivers are known hotspots for DOC processing [*Raymond et al.*, 2013]. This notion is further reinforced in a compilation of DOC losses during passages from terrestrial sources to sea, highlighting microbially mediated respiration of DOC in response to retention time scales [*Catalan et al.*, 2016]. Globally, streams and rivers are responsible for 1.8×10^{12} kg C yr^{-1} out of the total of 2.1×10^{12} kg C yr^{-1} CO_2 evasion from inland waters [*Raymond et al.*, 2013]. The total evasion has been revised upward to 3.9×10^{12} kg C yr^{-1} [*Drake et al.*, 2018],

owing to more observational data. However, this flux is likely an underestimation. Due to lack of hydrologic data in small-sized headwater streams, it has been suggested that C evasion from small streams may be substantial but remain unaccounted for [*Drake et al.*, 2018; *Raymond et al.*, 2013]. Here, we describe ambiguities in DOC processing associated with permafrost thawing and degradation first in lateral flow dominated Arctic watersheds, then in alpine watersheds with extensive surface water – groundwater interactions along the hillslopes.

The apparently wide variability in DOC processing observed in the Arctic permafrost regions can be reconciled by considering the evolving nature of the SOC sources and time it takes for the SOC leachate to infiltrate and move laterally into the stream (SOC to porewater DOC, then subsequently DOC in streams). All of these processes are likely to alter under ongoing climate change. Arctic river waters sampled at large basin scales (8000 to 855,000 km^2) have been shown to contain highly aromatic and less biologically labile DOC with young (390-1440 yr BP) radiocarbon age [*Balcarczyk et al.*, 2009; *Guo and Macdonald*, 2006; *Guo et al.*, 2007; *Kawahigashi et al.*, 2004]. This likely reflects inputs from modern active-layer soil SOC, as well as previously degraded Holocene permafrost SOC [*Heslop et al.*, 2019], plus further degradation along transport pathways due to long residence time of water in large basins [*Mann et al.*, 2015; *Spencer et al.*, 2015; *Striegl et al.*, 2005]. When permafrost SOC sources are ancient (> 20,000 yr BP) [*Drake et al.*, 2015] and terrestrial thaw process abrupt [*Turetsky et al.*, 2020], stream DOC can become more biologically labile, contributing significantly to in-stream C processing as evidenced by one third to one half of DOC losses in first-order tributaries of the Kolyma River basin [*Mann et al.*, 2015; *Spencer et al.*, 2015; *Vonk et al.*, 2013]. Field observations of soil C has indicated that half of SOC loss is attributable to the lateral flow passing into the aquatic system of the Eight Mile Lake watershed, though the further fate of the transported C is highly uncertain [*Plaza et al.*, 2019]. The need to understand how flow and water exchange regulate the quantity and quality of DOC reaching the stream is also clear from soil column experiments showing substantial (> 70%) C loss in lateral leachate with artificial precipitation [*Zhang et al.*, 2017]. Given the uncertainties associated with C cycling in small sized, lower order watersheds [*Raymond and Spencer*, 2015; *Raymond et al.*, 2013], it is useful to examine quantity and quality of DOC along the SOC to stream DOC transport pathways.

SOC transport pathways to streams are undergoing profound hydrological changes triggered by permafrost thawing [Mann et al., 2015; O'Donnell et al., 2012]. In Arctic permafrost

areas, there is an increasingly important role of groundwater linked with the increase of base flow and interaction between surface water and groundwater [*Connolly et al.*, 2020; *Frey and McClelland*, 2009; *Vonk et al.*, 2019]. Observations have identified accelerated input of older DOC exported as baseflow due to the deepening of flow path and increasing discharge [*Aiken et al.*, 2014; *Barnes et al.*, 2018; *Neff et al.*, 2006]. Warming is expected to reduce transit time, thus enhancing the propensity for lateral carbon transport along the terrestrial–aquatic continuum [*Vonk et al.*, 2019]. How changing hydrological processes will alter the in-stream C cycling in a warmer future is challenging to disentangle.

Assessing complex hydrological processes on catchment scales is a starting point to tackle such challenges. The Qinghai Tibetan Plateau (QTP) is an ideal location to study these processes as it contains the most extensive permafrost cover at the mid- and low- latitudes, but also because the spatially heterogenous degradation of permafrost following the topographical variation also influences hydrology [*Cheng and Wu*, 2007; *Yang et al.*, 2010]. Increasing precipitation and glacier melting have led to an expansion of water storage (12.1 ± 0.6 Gt yr^{-1}) [*Yi et al.*, 2016], especially that of groundwater storage (5.01 ± 1.59 Gt yr^{-1}) since 2003 [*Zhang et al.*, 2017]. Given such significant changes in QTP's hydrological cycle, it is likely that groundwater flow is affected [*Ge et al.*, 2011, *Yao et al*., 2017], yet few studies have examined such multifaceted changes and its biogeochemical implications. Recent advances in hillslope hydrology, especially the notion of groundwater mean transit time (MTT), defined as the time that water parcels spend between the time entering the unsaturated zone and the time flowing out of the aquifer [*Benettin et al.*, 2015; *McDonnell et al.*, 2010], offer a unique perspective to shed light on DOC processing in northern, alpine permafrost zones. Because MTT is found to range only from days to weeks [*Luo and Jiao*, 2019], challenging the long-held view that distribution of transit time ranging from years to decades in alpine hillslope hydrological condition [*McGuire et al.*, 2005], this short time scale makes it worthwhile to integrate groundwater into the terrestrial SOC – aquatic DOC continuum. How groundwater – surface water interaction in hillslopes of headwater regions of QTP influences the fate of SOC derived DOC through regulating groundwater transit time, and in turn, the carbon loss in headwaters, remains largely unexplored.

To illuminate the emerging and likely significant role that hillslope hydrological processes play in biogeochemical C cycling, this study seeks to shed light on DOC processing in a small (25 km^2), alpine (elevation 2960 to 4820 m a.s.l) watershed named Hulugou (HLGW)

152 located in the northeastern QTP (Fig. 1). The conservative tracers of ^{18}O and electrical
153 conductivity are used in an end-member analysis to ascertain the contribution of frost soil to
154 multiple types of waters and to illustrate the extensive and spatially variable surface water –
155 groundwater interactions in HLGW. The spatial and temporal variations in quantity and quality
156 of dissolved organic matter (DOM) are interpreted to indicate rapid and variable transit time in
157 part caused by changes in groundwater flow paths in response to the freeze-thaw cycle. Finally,
158 how the new constraints on rapid groundwater transit time in the alpine watersheds of the QTP
159 sets the stage for DOC loss in headwaters and its implications for hillslopes acting as DOC
160 processing hotspots are discussed.

161

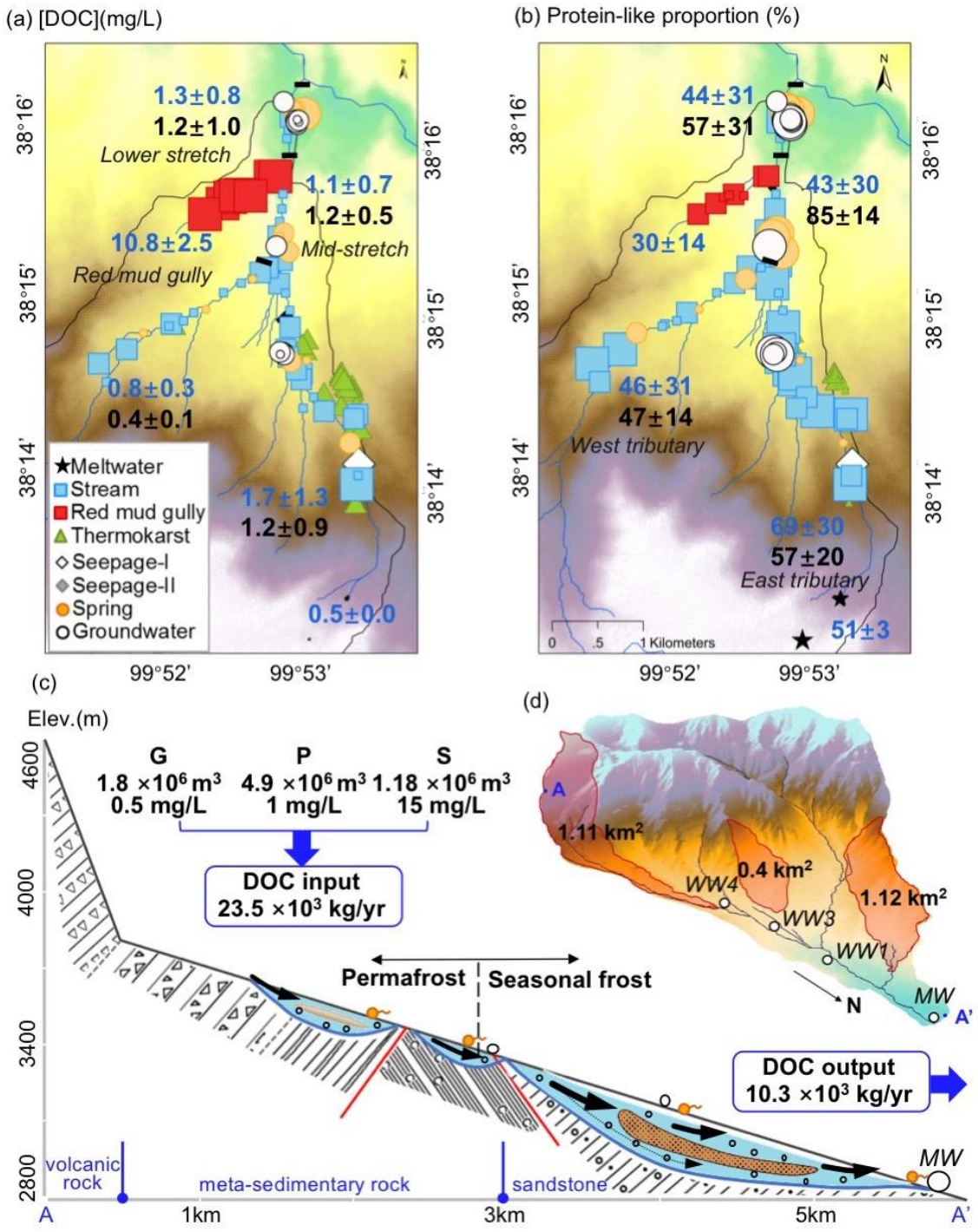

Figure 1. (a) Concentrations of DOC in eight types of water in HLGW, Qinghai-Tibetan Plateau, with legends in inserted panel. Small, medium and large symbol sizes indicate low (< 0.7 mg L^{-1}), medium (0.7-3.6 mg L^{-1}) and high (>3.6 mg L^{-1}) [DOC] according to its tertile values. Numbers are mean value ± one standard deviation for [DOC] in stream (blue) and subsurface water (black). **(b)** Proportions of protein-like component identified by PARAFAC modeling, with small, medium and large symbol sizes indicating low (<27.4%), medium (27.4–62.4%) and high (>62.4%) proportions according to tertile values. Numbers are mean value ± one standard

deviation for the proportion of protein-like compounds in stream (blue) and subsurface water (black). Maps of Other DOM optical properties $SUVA_{254}$, FI are available in Fig. S1. **(c)** A schematic diagram of hillslope hydrological process in HLGW for the cross-section A-A' (inset d, three areas of permafrost and seasonal frost in HLGW are shown, with monitoring wells marked in white circles). Water fluxes and [DOC] in three end members (G: glacier-snow melt, P: precipitation, S: frozen soil meltwater) contributing to DOC input are shown. The mass balance of DOC input and out fluxes suggests that about half of DOC is processed in HLGW.

2 Material and Methods

2.1 Study Area and Sample Collection

The study was conducted in Hulugou watershed (HLGW), upper Heihe basin, NE Qinghai-Tibetan Plateau (99°50′ – 99°54′ E, 38°12' – 38°17' N; 2960 to 4820 m a.s.l, 25 km^2). The HLGW consists of three geomorphic units of glacier-snow covered mountain, rocky hills, and meadow steppe. Glacier, permafrost and seasonal frost ground have experienced degradation, albeit to different extent within the HLGW [*Li et al.*, 2014]. A first-order stream network with extensive surface water and groundwater exchanges [*Chang et al.*, 2018; *Evans et al.*, 2015] is superimposed on permafrost (3400 m to 4500 m a.s.l) with abundant thermokarst ponds, seasonal frost ground (2900 m to 3400 m a.s.l), and degraded permafrost (3450 m to 3600 m a.s.l) with erosional channels (Fig. 1).

Water samples (n=129) were collected from HLGW for a total of five times in July 2012 (n=22), April (n=11), July (n=28) and September 2013 (n=30), and September 2018 (n=38), respectively. Eight types of water were sampled, including glacier-snow melt, streams, a thermo-erosional red mud gully, thermokarst ponds, seepage-I, seepage-II, spring and groundwater, with detailed sampling locations described in Table 1. All types of water samples except groundwater were collected from 2 cm below the surface. The meltwater sample was collected in triplicate at the same time from melting glacier-snow in bare gravel zone, and analyzed individually, with results reported as mean values of the triplicate samples that represent this one type of water. The upper-stretch of the stream network in HLGW includes the east and the west tributaries originating at elevation above 4765 m. After the east and the west tributaries converge, the mid-stretch flows through the permafrost zone into the seasonal frozen soil zones, and becomes the lower-stretch after the red mud gully joins in (Fig. 1). Red mud gully is an erosional tributary; formed by water cutting deeply into the seasonal frost ground in the alpine meadow between

3300 m to 3000 m a.s.l, and thus classified separately as a type of water. Thawing of permafrost results in many small thermokarst ponds (diameter < 1 m mostly), observed in the alpine meadow at an altitude ranging from 3351 m to 3548 m close to the east tributary. The aquifer lithology and the installation of the observation wells are described in a previous study [*Hu et al*., 2019]. Groundwater samples were collected from the wells shown in Fig. 1d with well depths being WW1–25 m, WW3–5 m, WW3–10 m, WW3–20 m, WW3–30 m and MW–30 m (Fig. 1d), after the wells have been primed until stable readings of temperature and EC were reached.

Cation and anion samples were filtered with 0.22 μm nylon filters. Stable isotopes $H_2{}^{18}O$ and D_2O samples were filtered with 0.22 μm nylon filters into 2 ml glass bottles then immediately sealed without head space. Dissolved organic matter (DOM) samples were filtered using glass fiber syringe filters (Whatman GF/F style) with a 0.7 μm nominal pore size into pre-combusted (at 450 °C for 6 hours) 22 ml brown glass bottles and crimp sealed with Teflon-faced silicone septa. All samples were filtered immediately after sampling and stored on ice at 4°C for shipment to laboratory.

2.2 Measurements of field and chemical parameters, stable isotopes and DOM

Temperature (T), electrical conductivity (EC), pH and alkalinity were measured in the field. Stable isotopes (δD and δ^{18}O) were measured on a water isotope spectrometer analyzer (Model PICARRO L2130-I) at Pri-ecoco, Beijing, China (see Text S1 of Supporting Information). Major anions and cations of samples in 2012 and 2013, were measured by ion chromatography (IC-1000, Dionex) and Inductively Coupled Plasma Atomic Emission Spectroscopy (ICPAES, Teledyne Leeman, Prodigy), respectively. Major ions of sample in 2018 were measured on IC (Aquion, Dionex) with CS18 analytical column for anions, and CS16 column for cations, respectively. DOC concentrations of all water samples and soil extraction solutions (see Text S2 and Fig. S2 of Supporting Information on soil incubation) were measured on a Shimadzu TOC Analyzer. Detailed procedures are in Text S1 of Supporting Information.

Absorbance of UV-Visible chromophore DOM (CDOM) was measured by a UV-Visible Spectrophotometer (Agilent 8453) scanning from 200 to 800 nm (1 nm increments) to acquire absorbance for samples collected in 2012 and 2013. Prior to analyzing samples, a quartz cuvette filled with Milli-Q water was used to establish a daily baseline. Excitation emission matrices

(EEMs) were employed by scanning over an excitation (ex) range of 240 to 450 nm at 10 nm increments, and an emission (em) range of 350 to 550 nm at 2nm increments on a JY-Horiba Fluoromax-3 spectrofluorometer (Queens College, CUNY) with instrument-specific corrections, Raman normalization, inner filter correction, and cuvette blank subtraction applied. Optical properties of samples collected in 2018 were analyzed using a Horiba Aqualog spectrofluorometer (Southern University of Science and Technology) following the same procedure. EEMs were generated over excitation wavelengths between 246.58 to 827.57 nm in about 1.2–nm interval and emission wavelengths between 220 to 800 nm in 1-nm interval. All DOM measurements were completed within two weeks of sampling.

To correct for minor effect of light scattering by particles and microbubbles, wavelength-independent correction is conducted by subtracting the mean absorbance at range of 600 to 800 nm from all spectral absorbance values [*Green and Blough*, 1994]. Specific UV absorbance (SUVA) represents relative DOM aromaticity [*Weishaar et al.,* 2003], and SUVA at 254 nm ($SUVA_{254}$) was applied in this study following previously reported methods [*Weishaar et al.*, 2003]. Fluorescence index (FI) is calculated as the ratio of intensities emitted at 470 nm and 520 nm at an excitation wavelength of 370nm, with lower value (~1.2) usually indicating for more terrestrial derived DOM and higher (~1.8) for more microbial DOM sources [*Cory and McKnight*, 2005; *McKnight et al.,* 2001]. Freshness index (BIX) is calculated as the ratio of emission intensity at 380 nm to the maximum intensity between 420 nm and 435 nm at an excitation wavelength of 310 nm [*Parlanti et al.*, 2000]. Higher value of BIX represents a higher proportion of fresh DOM [*Parlanti et al.*, 2000].

Table 1. Description of water types, electrical conductivity (EC), isotopic compositions, DOC concentration and optical properties in eight types of water in HLGW sampled between 2012-2018.

Description	Elevation range (m)	Types of water in HLGW	n	EC ($\mu s\ cm^{-1}$)	$\delta^{18}O$ (‰)	δD (‰)	DOC ($mg\ L^{-1}$)	Protein proportion (%)	$SUVA_{254}$ ($L\ mgC^{-1}\ m^{-1}$)	FI	BIX
Melting glacier-snow in bare gravel zone	4100	Meltwater	1	179±1	-10.6±0.5	-64.8±3.8	0.5±0.0	51±3	0.33±0.17	1.94±0.04	0.83±0.02
Upper-, mid-, and lower-stretch *	3620-2920	Stream	41	355±141	-9.1±0.4	-52.1±4.6	1.3±1.1	56±33	1.09±0.63	1.62±0.16	0.73±0.14
Erosional tributary cutting through the seasonal frost zone	3200-3050	Red mud gully	10	2881±399	-6.3±0.4	-32.8±2.5	10.8±2.5	30±14	2.84±0.78	1.50±0.14	0.71±0.09
Seasonal frost ground in alpine meadow	3620-3350	Thermokarst ponds	26	334±123	-4.5±0.7	-24.8±5.3	14.3±3.3	24±11	3.75±0.48	1.37±0.09	0.59±0.05
Emerging thermokarst	3610	Seepage-I	2	322±25	-6.4±0.1	-37.1±0.6	7.1±1.0	45±22	3.16±0.35	1.29±0.04	0.58±0.03
Slow discharging spring	3410-3060	Seepage-II	4	501±181	-9.1±0.4	-52.2±2.0	1.5±0.8	43±39	1.16±0.80	1.60±0.16	0.61±0.12
Fast discharging spring	3570-2950	Spring	17	450±196	-8.7±0.3	-50.1±2.2	1.1±1.0	59±31	1.14±0.60	1.75±0.21	0.74±0.21
Six wells‡	3300-2970	Groundwater	13	573±61	-8.5±0.3	-48.0±2.1	1.0±0.4	62±24	0.88±0.45	1.82±0.14	1.12±0.38

* Upper-stretch includes east and west tributaries and is in permafrost zone, mid-stretch is in seasonal frost zone, and the lower-stretch is in seasonal frost zone

‡ Wells shown in Fig. 1d with depths being WW1–25 m, WW3–5 m, WW3–10 m, WW3–20 m, WW3–30 m and MW–30

2.3 Parallel Factor Analysis (PARAFAC) of DOM Fluorescence Spectra

Fluorescence spectra, obtained as EEMs, are used to quantify the contribution of fluorescent DOM components through PARAFAC modeling [*Coble*, 1996; *Murphy et al.*, 2013]. PARAFAC was conducted following the procedures described in a previous algorithm to quantify the protein-like fluorophores and humic-like substances of DOM [*Murphy et al.*, 2013; *Stedmon and Bro*, 2008]. Prior to outlier tests, the intensity of EEMs of samples in 2018 was linearly interpolated to match the emission ranging 250 to 450 nm at an interval of 10 nm and excitation ranging 300 to 550 nm at an interval of 2 nm. To avoid highly fluorescent samples exerting significant leverages on the PARAFAC model, normalization of each EEM to its integrated fluorescence was applied before model fitting [*Murphy et al.*, 2013]. Normalized fluorescence of each EEM was reversed to its raw fluorescence after model fitting.

We applied two PARAFAC models with two datasets. The first model includes all 100 water samples and the second adds 47 soil extracted samples to the first dataset of 100 water samples (see Section 2.7 on soil extraction). A series of three to six component- models were fitted to the dataset, with non-negativity constraint of 10^{-8} applied to each. The split-half validation was achieved through splitting the data in half and modeling each half separately, fitting 20 models with random starts, and by inspection towards lowest residuals [*Murphy et al.*, 2013]. The PARAFAC analysis resolved a four-components model comprising the EEMs dataset, explaining 97.8% of the total variance. The comparisons of two model exports are shown in Figure S6, suggesting consistency with additional samples. Spectra loadings of both excitation and emission mode for each component were matched to the OpenFluor database (https://openfluor.lablicate.com/of/measurement/1104), and the description of each component was interpreted from matched compounds identified from previous studies with similarity >95% [*Murphy et al.*, 2014]. The identified four fluorescence components (C1 to C4) are ubiquitous and common in marine environments [*Catala et al.*, 2015; *Wunsch et al.*, 2018], as well as cryosphere such as Arctic surface waters [*Gonçalvesaraujo et al.*, 2016] and ice cores in Arctic Canada [*Brogi et al.*, 2018], and ice in the Antarctic seas [*Stedmon et al.*, 2011]. The C1 and C3 components have a broader emission spectrum and two extraction spectra peaks, traditionally referred to as humic-like components (Fig. S3). The C2 (ex: 270 nm; em: 304 nm) and C4 (ex: 290 nm; em: 338) components have narrower spectra with excitation and emission maxima

below 350 nm (Fig. S3), and are similar to the spectra of tyrosine and tryptophan, respectively [*Murphy et al.*, 2008]. The characterization of C2 and C4 represents amino-acids, free or bound in proteins compounds. The proportion of protein-like fluorophores is calculated as the sum of C2 and C4 intensities divided by the bulk intensity of the sample. Representative EEMs of different water types are enclosed in Supporting Information (Figs. S4 and S5).

2.4 End Member Analysis Based on Conservative Tracers

A three end-member mixing analysis constrained by conservative tracers $\delta^{18}O$ and EC was used to calculate the fractions of glacier-snow (f_G), precipitation (f_P) and frozen soil melt water (f_S) contributing to stream and subsurface waters in HLGW. The same three end members have been adopted in a hydrograph separation study of HLGW [*Li et al.*, 2014]. The analysis is based on the following assumptions: (1) the three water sources are the dominant sources over the ablation season and that any other sources are negligible; (2) shallow, organic layer of frozen soil is involved in lateral flow thus provides a signature needing representation.

$$f_G \times C_G^{18O} + f_P \times C_P^{18O} + f_S \times C_S^{18O} = C_i^{18O} \quad (1)$$

$$f_G \times C_G^{EC} + f_P \times C_P^{EC} + f_S \times C_S^{EC} = C_i^{EC} \quad (2)$$

$$f_G + f_P + f_S = 1 \quad (3)$$

where f represents the estimated fraction of a given endmember contributing to the specific sample i; the subscripts G, P and S represent the glacier-snow meltwater, precipitation and soil endmember, respectively; C^{18O} and C^{EC} represent the $\delta^{18}O$ and EC of the sample specified in the subscript, respectively.

The $\delta^{18}O$ and EC values to constrain the glacier-snow endmember composition rely on not only a meltwater sample collected in triplicate and analyzed individually in this study, but also two newly deposit snow samples collected in May and November of 2012 and one meltwater sample collected in July 2012 in the front of a glacier in HLGW [Li et al., 2015] (Table 2). The elevation-weighted $\delta^{18}O$ (-7.66‰) and the volume-weighted $\delta^{18}O$ (-7.7‰) are comparable based on 65 rainwater samples collected weekly between June 28 to Sept 2, 2012 from 7 elevations (2960 to 4160 m a.sl.) of the HLGW [*Chang et al.*, 2018]. The volume-weighted $\delta^{18}O$ becomes more negative with higher elevation at a rate of 0.19‰ per 100 m in HLGW [*Chang et al.*, 2018]. The volume-weighted mean EC and $\delta^{18}O$ are used to represent the precipitation endmember

(Table 2). In July 2013, pore waters were collected from piezometer installed to depths of 0.6 m to 1.5 m; groundwater was collected from monitoring well WW4 with a depth of 1 m. These 3 samples were regarded to represent frozen soil water [*Li et al.*, 2014; *Ma et al.*, 2017]. The EC and $\delta^{18}O$ endmember compositions were averaged from these samples plus 87 samples collected underneath 7 soil profiles at elevation between 3620 to 2920 m analyzed similarly in *Li et al* [*Li et al.*, 2014] (Table 2).

To estimate the uncertainty associated with the tracer-based end-member analysis, a classical Gaussian error propagation equation was employed [*Genereux*, 1998]. The calculation followed procedure described elsewhere [*Chang et al.*, 2018]. The fractions and associated uncertainties are reported in Table 2 and Table S1.

$$W_f = \left[\left(\frac{\partial f}{\partial C_G^{18O}} W_G^{18o}\right)^2 + \left(\frac{\partial f}{\partial C_P^{18O}} W_P^{18o}\right)^2 + \left(\frac{\partial f}{\partial C_s^{18O}} W_s^{18o}\right)^2 + \left(\frac{\partial f}{\partial C_i^{18O}} W_i^{18o}\right)^2 + \left(\frac{\partial f}{\partial C_G^{EC}} W_G^{EC}\right)^2 + \left(\frac{\partial f}{\partial C_P^{EC}} W_P^{EC}\right)^2 + \left(\frac{\partial f}{\partial C_s^{EC}} W_s^{EC}\right)^2 + \left(\frac{\partial f}{\partial C_i^{EC}} W_i^{EC}\right)^2\right]^{1/2} \quad (4)$$

where *W* represents the uncertainty in the variable specified in the subscript, i.e W_f represents the uncertainty of the contribution fraction for a given end member in a sample, W_G^{18o} represents the uncertainty of $\delta^{18}O$ in glacier-snow endmember.

2.5 Estimation of DOC Loss: ΔDOC

Because DOC is non-conservative, we first estimate an initial DOC (DOC_0) through summation of DOC contributed from each endmember (equation 5).

$$DOC_0 = f_G \times DOC_G + f_P \times DOC_P + f_S \times DOC_S \quad (5)$$

The DOC concentration (0.5 ± 0.02 mg L^{-1}) in meltwater at the highest elevation is taken to represent the glacier-snow endmember (Table 2). The DOC concentration (15 ± 2.5 mg L^{-1}) of pore water samples collected by piezometers is taken to represent the soil endmember (Table 2). Though DOC of rainfall was not measured in HLGW, the volume-weighted mean DOC is 0.9 mg L^{-1} in three remote meteorological stations and 1.1± 0.5 mg L^{-1} in Lhasa city of central QTP [*Li et al.*, 2017; *Li et al.*, 2018]. The DOC of 1.0 mg L^{-1} is taken to represent the precipitation endmember (Table 2).

The difference between initial DOC and measured DOC of a sample suggests the loss of carbon along the flow path of water to the sampling point. The DOC loss (ΔDOC) is calculated by subtracting measured DOC concentration ([*DOC*]) of a given water sample from its initial DOC (DOC_0) calculated above, where larger ΔDOC corresponds to more loss of DOC during transport.

$$\Delta DOC = DOC_0 - [DOC] \quad (6)$$

Table 2. Mean and standard deviation (mean ± std) of $\delta^{18}O$ (‰) and electrical conductivity (EC, μS/cm) used in computing end-member mixing fractions and their uncertainties (*W*), and DOC (mg/L) in the three end members.

End-member	$\delta^{18}O$ (‰)				EC (μS/cm)				DOC (mg/L)
	mean ± std	n	t^* (0.7)	W^{18o} (0.7)	mean ± std	n	t^* (0.7)	W^{EC} (0.7)	mean ± std
Glacier-snow meltwater	-14 ± 3.9	6	1	3.9	160 ± 27	4	1	27	0.5±0.02
Precipitation	-7.7 ± 2.0	65	0.85	1.7	35 ± 3.0	65	0.85	2.5	1
Frozen soil meltwater	-5.3 ± 0.2	3	1	0.2	3487 ± 542	4‡	1	542	15 ± 2.5

* *The uncertainty of each tracer in a specific endmember is calculated as the standard deviation multiplying the t value under coefficient level at 0.7.*

‡ *The mean value of EC is averaged from three endmember samples and the average EC value of 87 soil samples from Li et al., [2004].*

2.6 Estimation of Groundwater Mean Transit Time

First order kinetics have been widely used to describe biodegradation of DOC incubation experiments [*Catala et al.*, 2015], allowing for calculation of the degradation rate constant (λ) as in equations (7), where the DOC_0 usually represents the starting point of the experiment.

$$DOC = DOC_0 \times e^{-\lambda t} \quad (7)$$

Because photodegradation is unlikely in subsurface environment, the biodegradation rate constant is assumed to regulate DOC degradation in groundwater. Re-arranging equation (7) to simulate the ΔDOC change in groundwater observed at the outlet of HLGW in July and September result in equation (8), with the calculated time, t, regarded as representing groundwater mean transit time (MTT). The assumptions for the linkage between DOC loss behavior and transit time are (1) photodegradation is negligible in subsurface environment; (2)

the potential direct input from particle organic carbon along the pathway is excluded because particles would not be transported by groundwater; (3) physical removal of DOC due to retardation is expected to be fast, evenly distributed and hence not considered.

$$1 - {\Delta DOC}/{DOC_0} = e^{-\lambda_{gw} t} \quad (8)$$

$$MTT \approx t = -\frac{\ln\left(1 - {\Delta DOC}/{DOC_0}\right)}{\lambda_{gw}} \quad (9)$$

where λ_{gw} represents DOC degradation constant in groundwater which has been corrected to observed groundwater temperature of 5 ^{o}C based on the Arrhenius equation [*Catalan et al.*, 2016] from the incubation experiment temperature of 20 ^{o}C.

2.7 Soil Incubation Experiment

A batch incubation experiment of SOC was initiated in the field to minimize sample storage artifacts. Four soil profiles were sampled at elevations from 2850 to 3600 m a.s.l and included seasonal frozen soil, thermokarst ponds and less degraded permafrost soil (Table S2). Approximately 5 g of soil was weighed and added to pre-combusted 20-ml glass bottles in triplicate, and filled with 15 – 19 ml Milli-Q water. Then the bottles were crimp sealed with Teflon-coated septa and aluminum cap right away. The bottles were stored in room temperature in dark before the supernatant was sampled at day 1, 3 and 40, sacrificing a bottle at a sampling time. The supernatant was filtered and measured for DOC concentrations, UV-visible absorbance and fluorescence spectra were performed within a week of sampling following the same protocol as in section 2.2.

A second incubation experiment used a reactor approach similar to Drake et al to evaluate the biodegradation rate of soil derived DOC [*Drake et al.*, 2015] (Fig. S2). The shallow frost sample was collected by excavation to reach a depth of 50 cm within the active layer with thickness of 2 m nearby the well WW4. The sample was kept and transported on ice in a cooler to the lab. The details of incubation set up and sampling were described in Text S2 of supporting information.

3 Results

3.1 Frozen Soil Meltwater Contributes to All Water Types

Stable isotope characteristics of eight types of water indicate the influence of not only glacier-snow meltwater (G) and precipitation (P) but also frozen soil melt water (S) endmembers (Figs. 2a and 2b). Stream and subsurface water (groundwater, spring and seepage-II) samples fall within the triangle defined by the G, P and S endmembers (Figs. 2a and 2b). The regression line of meltwater, stream, seepage-II, spring and groundwater ($8.07 \times \delta^{18}O + 20.79$, r^2=0.92, n=71, blue line in Fig. 2a) is similar to the local meteoric water line (LMWL: $8.5 \times \delta^{18}O + 22.6$, gray line in Fig. 2a) of HLGW [*Ma et al.*, 2017]. In contrast, thermokarst pond waters, two seepage-I samples and red mud gully waters exhibit more positive isotopic compositions and fall below the local meteoric water line (LMWL) on a different trend line ($5.16 \times \delta^{18}O - 1.13$, r^2=0.83, n=20, black line in Fig. 2a), indicating fractionation due to evaporation [*Froehlich et al.*, 2008]. The red mud gully waters are most similar to the frozen soil melt water endmember in compositions (Fig. 2b); and this is interpreted to indicate that red mud gully waters are derived from the frozen soil melt water. The two seepage-I samples (emerging thermokarst) represent mixing between roughly 25%±1% of the soil endmember, and 75%±1% of the precipitation endmember, respectively (Fig. 2b). The thermokarst pond waters are also likely a mixture of the S and P endmembers, although the $\delta^{18}O$ values have become more positive due to evaporation. In summary, red mud gully, emerging thermokarst (seepage-I) and thermokarst ponds all have significant frozen soil meltwater contribution.

Using EC and $\delta^{18}O$ to un-mix among the three endmembers for stream and subsurface water (groundwater, spring, and seepage-II) samples falling within the triangle, precipitation contributes on average about 62%±7%, 64%±4%, 61%±4% and 63% of the water in stream, groundwater, spring, and seepage-II, respectively (Fig. 2b). Glacier-snow meltwater ranked second for stream (28%±6%), groundwater (18%±4%) spring (24%±4%) and seepage-II (26%) contributions. Frozen soil meltwater contributed the least to the stream waters (10%±4%), but contributed 11%, 15%±5%, and 17%±2% in seepage-II, spring, and groundwater samples, respectively.

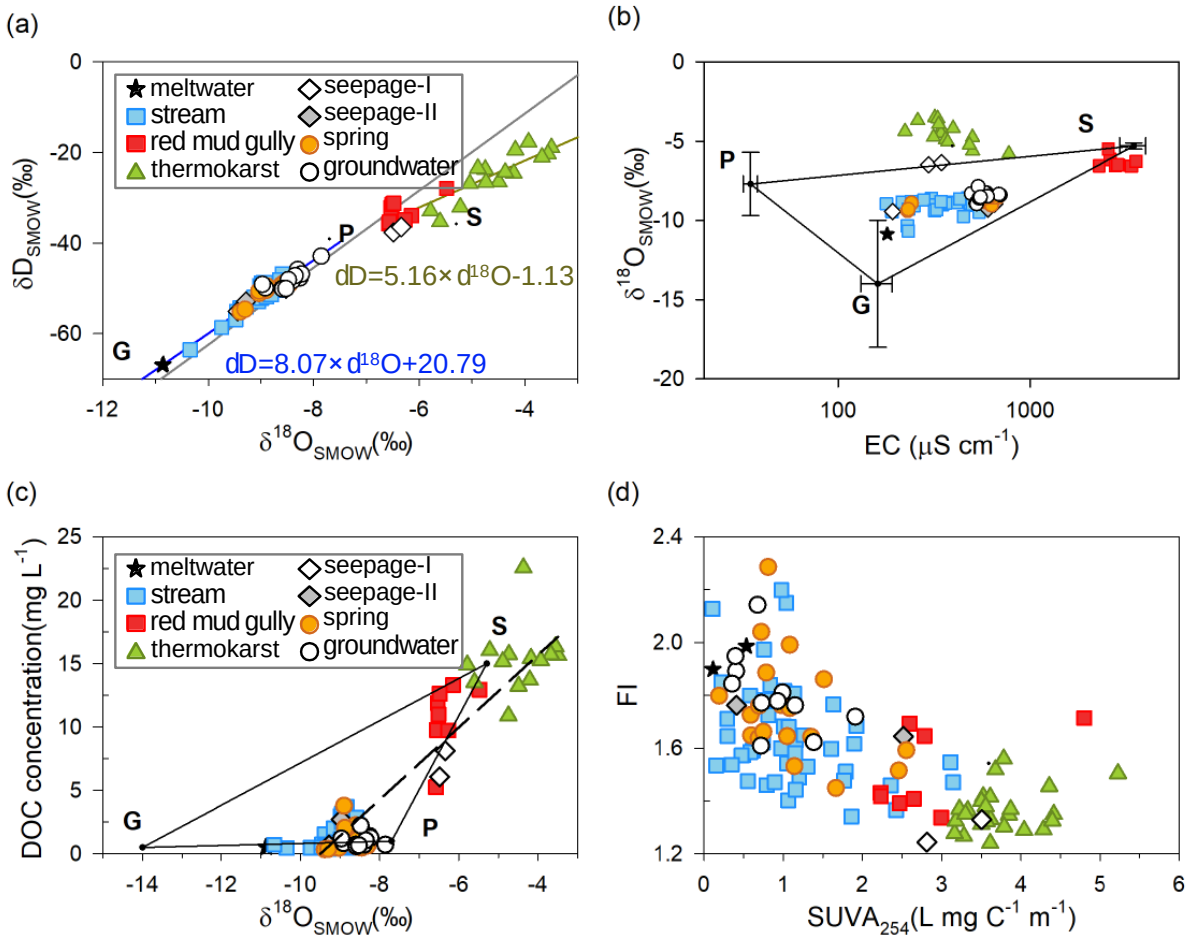

Figure 2. (a) Stable isotope compositions ($\delta^{18}O$ and δD) of eight types of water in HLGW. Three endmembers: glacier-snow meltwater (G), precipitation (P) and frozen soil meltwater (S) are marked according to their compositions. Local meteoric water line (LMWL: 8.5 × $\delta^{18}O$ + 22.6) is shown as a gray line [*Ma et al.*, 2017]. (b) The $\delta^{18}O$ vs electrical conductivity (EC, log scale) of eight types of water samples from HLGW. The triangle outlines the three end members with the error bar representing standard deviation for the two tracers. Uncertainties in $\delta^{18}O$ and EC of the three endmembers are reported in Table 2. (c) The $\delta^{18}O$ vs DOC concentrations for all eight types of water within HLGW are shown with a positive correlation (p < 0.01; n = 103). The triangle outlines the three end members according to their $\delta^{18}O$ and DOC concentrations. (d) The $SUVA_{254}$ vs FI for all eight types of water with a negative correlation (r = – 0.59, p = 0.01).

3.2 Frozen Soil Thaw Supplies the Majority of DOM to Surface and Subsurface Waters

Several lines of evidence suggest that DOM in surface water has been influenced by DOM from thawing of seasonal frost and/or permafrost. Three types of water show high DOC levels (Table 1): thermokarst ponds (14.3 ± 3.3 mg L^{-1}), red mud gully (10.8 ± 2.5 mg L^{-1}) and seepage-I (7.1 ± 1.4 mg L^{-1}). The elevated DOC levels of these three types of water are consistent

with the large contribution of frozen soil melt water endmember (Fig. 2b). These waters also show the most positive $\delta^{18}O$, with a correlation with DOC concentrations (Fig. 2c). Because DOC concentrations in glacier-snow melt (0.5 mg L^{-1}) and precipitation (1 mg L^{-1}) endmembers are low, this means that DOC in the stream (1.3 ± 1.1 mg L^{-1}, spring (1.1 ± 1.1 mg L^{-1}), groundwater (1.1 ± 0.4 mg L^{-1}) and seepage-II (1.5 ± 0.8 mg L^{-1}) must include a source from thawing of frozen soil, consistent with the water source analysis results above. When the DOC concentrations of all samples are divided according to the two tertile values, with one third of samples each belonging to low, medium and high levels equally (Fig. 1a), stream waters (n = 29) with low DOC level (0.7 ± 0.3 mg L^{-1}) display the most negative $\delta^{18}O$ values of –9.20 ± 0.48 ‰ while stream waters (n = 12) with medium DOC level (2.9 ± 0.7 mg L^{-1}) show in-between $\delta^{18}O$ of –8.82 ± 0.14 ‰, indicating input of frozen soil-derived DOC to streams.

Further support for the importance of thawing supplied DOM in the watershed is based on characterization of the quality of DOM by UV-visible and fluorescence spectroscopy because of its ability to absorb light and fluoresce. The optical properties including $SUVA_{254}$, FI and BIX all point to various degrees of influence by DOM from thawing of seasonal frost and/or permafrost soil. Thermokarst, red mud gully and seepage-I (emerging thermokarst) waters characterized by elevated DOC concentration display the highest $SUVA_{254}$ and the lowest FI values (Fig. 2d and Table 1). This indicates overwhelming influence by terrestrial plant-soil sourced DOM with high aromaticity from organic matter produced some time ago. The glacier-snow meltwater is the least likely to be influenced by any DOM from frozen soil melt, and thus shows the lowest $SUVA_{254}$ (0.33±0.17 L mgC^{-1} m^{-1}) and the highest FI (1.94±0.04). Stream, spring and groundwater display $SUVA_{254}$ and FI values between the aforementioned two DOM optical "endmembers" (Fig. 2d). Subsurface waters (spring and groundwater) show higher BIX and FI values than stream water, indicating recent microbially processed DOM [*Parlanti et al.*, 2000], consistent with the interaction with microbes in subsurface environment. The BIX values of meltwater, groundwater, and most spring water lie above the median BIX value of 0.69 of the all eight types of water, while those of most stream, red mud gully, seepage-I and thermokarst pond waters are below (Fig. S6).

3.3 Differences in DOM Quality in Surface and Subsurface Waters Support Subsurface Processing

The DOM of meltwater collected at the origin of the east tributary displays low $SUVA_{254}$ of 0.33±0.17 L mg C^{-1} m^{-1} and 51±3% of protein-like fluorophores based on a four-component PARAFAC model quantifying fluorescent DOM composition (Figs. 1b and Table 1). These values are comparable to that of glacier-snow meltwater (n=2) in southwest QTP, with $SUVA_{254}$ of 0.60 L mg C^{-1} m^{-1} and >50% of amino-acids [*Spencer et al.*, 2014; *Xu et al.*, 2013]. Although the meltwater can be a source of bioavailable DOC based on FT-ICR-MS analysis with high proportions of protein-like fluorophores [*Feng et al.*, 2016], its DOC concentration is also the lowest among the eight types of water. Thus, there must be additional DOC with such optical properties from other sources. Three types of water with significant S contribution, including thermokarst, red mud gully and seepage-I, contain high DOC with substantial (though variable) proportions of protein-like fluorophores of 24±11% (n=12), 30±14% (n=8), and 45±22% (n=2), respectively (Table 3). The permafrost SOC fingerprints evident in these three types of water are also observed in stream, spring and groundwater with DOM containing substantial though spatially variable proportions of protein-like fluorophores (Fig. 1b), intermediate $SUVA_{254}$ of ~ 1 L mgC^{-1} m^{-1} and medium-to-high FI of > 1.6 (Fig. S6).

Several lines of evidence support that differences in water – permafrost soil hydrological interactions in the upper-, mid-, and lower-stretches of the HLGW lead to spatial variations in DOM quality in surface and subsurface waters. In the upper-stretch, the quantity and quality of DOC in surface water exhibit notable differences between the east and the west tributaries. Concentrations of DOC and proportions of protein-like components are on average higher in the east tributary (1.7±1.3 mg L^{-1}, 69±30%) that drains two areas of permafrost and seasonal frost areas than those in the west tributary (0.8±0.3 mg L^{-1}, 46±31%) that drains only one smaller area of permafrost (Fig. 1d and Table 3). Subsurface waters of the upper stretch display lower DOC concentration than surface water (Fig. 1a), with slightly less protein-like proportions and higher $SUVA_{254}$ (Fig. 1b and Table 3).

From the mid-stretch to the outlet of the HLGW, the quality of stream DOC reflects mixing of upstream waters from the east and west tributaries, and after convergence of red mud gully, with this additional input (Fig. 1a and Table 1). The comparable subsurface water DOC

mean concentrations between the upper-stretch east tributary (1.2±0.9 mg L^{-1}) and lower- (1.2±1.0 mg L^{-1}) stretches (Table 3) suggests that a groundwater flow path may connect the highest elevation area in the east with the lowest elevation area (Figs. 1a and 1b). The mid-stretch subsurface water may have been influenced more by a cluster of thermokarst ponds nearby because the proportion of protein-like fluorophores (85±14 %, n=4) in four subsurface water samples from the mid-stretch nearly double that of stream water, with higher $SUVA_{254}$ values as well (Fig. 1b and Table 3). This may be attributed to less photodegradation of permafrost sourced DOM in subsurface environment than in surface water.

In each stretch of the HLGW stream network, the mean value of FI in subsurface waters is substantially higher than that in the surface waters (Table 3), indicating more microbially processed DOM in subsurface environment, except for the mid-stretch where subsurface processing may be weak. When protein-like proportion is divided into three groups again according to the two tertile values, all of 12 groundwater samples, and 10 out of 13 spring samples belong to medium and high levels (Fig. 1b). The spring waters also have the highest bulk fluorescence intensity averaging 3.85 ± 6.58 RU (Dataset S1). Taken together, the differences in DOM quality in surface and subsurface waters, along with the spatially variable distribution of optical properties of DOM, suggest that subsurface environment actively participate in DOM processing in headwaters of the QTP, with microbially driven biodegradation likely being important (see section 4.1).

Table 3. DOC concentrations, optical properties of DOM, proportions of glacier-snow (f_G), precipitation (f_P) and soil water (f_S) contributing to stream and subsurface waters and associated DOC loss for the upper, mid and lower stretches of HLGW.

Category	Type*	n	DOC (mg/L)	Protein proportion (%)	$SUVA_{254}$ (L mg C^{-1} m^{-1})	FI	f_G	f_P	f_S	DOC_0 (mg/L)	ΔDOC (mg/L)
Upper stretch: east tributary (3620-3190 m)	surface	21	1.7±1.3	69±30%	1.18±0.60	1.60±0.14	29±9%	62±9%	10±4%	2.2±0.6	1.2±0.8
	subsurface	9	1.2±0.9	57±20%	1.38±0.73	1.71±0.11	19±2%	64±4%	17±2%	3.3±0.3	2.3±0.5
Upper stretch: west tributary (3500-3180 m)	surface	13	0.8±0.3	46±31%	1.12±0.75	1.62±0.20	27±3%	65±3%	8±2%	2.0±0.3	1.2±0.5
	subsurface	3	0.4±0.0	47±14%	1.00±0.37	1.85±0.15	27±4%	59±5%	13±6%	2.7±0.8	2.3±0.8
Mid-stretch (3140-3040 m)	surface	8	1.1±0.7	43±30%	0.77±0.24	1.66±0.10	27±3%	58±3%	16±2%	3.0±0.3	1.9±0.5
	subsurface	4	1.2±0.5	85±14%	1.00±0.16	1.69±0.18	22±3%	64±3%	14±5%	2.9±0.8	1.7±0.9
	surface	3	1.3±0.8	44±31%	0.76±0.21	1.67±0.12	26±2%	60±5%	14±3%	2.8±0.4	2.4±0.1

Lower stretch (3000-2940 m)	subsurface	13	1.2±1.0	57±31%	0.81±0.40	1.84±0.21	22±4%	62±4%	15±3%	3.1±0.5	2.2±0.7

[*]*Note. Surface represents stream and subsurface includes spring and groundwater. Data are reported as averages ± standard deviation for each category.*

3.4 Concurrent DOC Quantity and Quality Changes in Stream and Subsurface Waters

The loss of DOC (ΔDOC) in stream and subsurface waters, calculated by subtracting the measured DOC concentration from an estimated initial DOC concentration based on mixing of three-endmembers, represents DOC consumption along the flow paths in HLGW. In subsurface waters where the effect of photodegradation is minimal, simultaneous decreases in the proportions of protein-like fluorophores and $SUVA_{254}$ values are observed with increasing ΔDOC (Fig. 3). For the stream waters, only the proportion of protein-like fluorophores is correlated with ΔDOC, not $SUVA_{254}$ (Fig. 3). If only the upper stretches of the stream network in HLGW are considered, the correlations between the proportions of protein-like fluorophores and ΔDOC improve in the about 2-km long east ($r = -0.73$, $p = 0.002$) and west ($r = -0.78$, $p = 0.003$) tributaries, respectively. The lack of correlation between stream water $SUVA_{254}$ and ΔDOC (Fig. 3) is likely due to stronger effect of photodegradation in surface water than in groundwater due to aromatic C as light absorbing chromophores [*Ward and Cory*, 2016].

The concurrent changes in DOC quantity and quality are observed in the batch experiments of four types of frozen soils collected from the HLGW. Consistent with the concurrent changes in DOM quantity and quality in HLGW waters (Fig. 3), anoxic incubation of four types of soil reveals utilization of protein-like components and aromatic carbon. Decrease of $SUVA_{254}$ from > 4 to about 1 L mg C^{-1} m^{-1} and halving of protein-like fluorescent DOM is found in 8 soil samples collected from the active layers of permafrost, the degraded permafrost and thermokarst soils (Table S2). However, the soil incubations are compounded by simultaneous release of DOM from SOC mobilization, and adsorption may also contribute to DOC loss, making quantitative assessment impossible at this time, with details in Supporting Information. When the first-order kinetic equation was applied to fit the SOC biodegradation curves for the decrease in DOC in the second incubation experiment of the frost soil in the reactor, the biodegradation constant of SOC (λ_{SOC}) is estimated to be 0.32 d^{-1} at 20 ºC, or a half-time of 5 hours (Fig. S7).

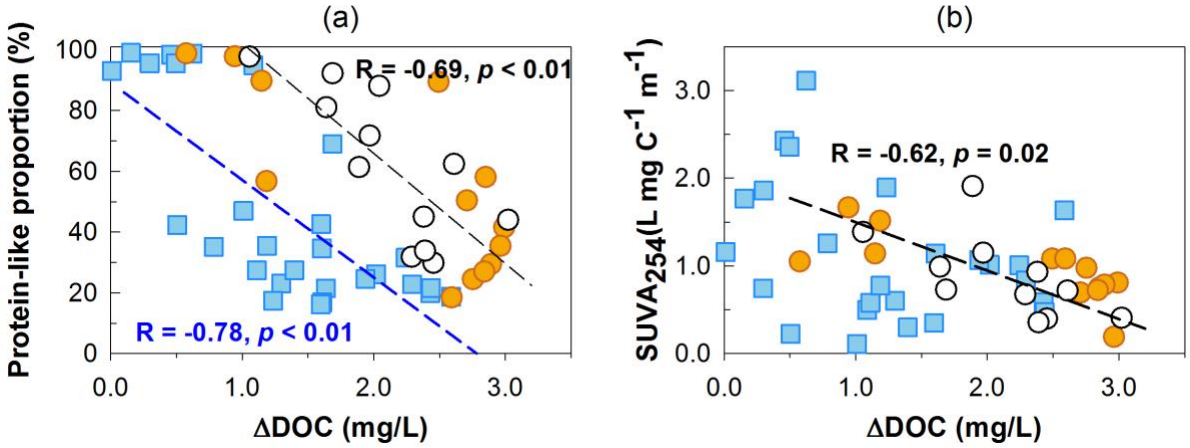

Figure 3. (a) The proportion of protein-like component vs DOC loss (ΔDOC) in surface (blue) and subsurface (white and orange) water. (b) $SUVA_{254}$ vs DOC loss (ΔDOC) in surface (blue) and subsurface (white and orange) water. The blue and black dash lines represent the regression lines for stream and groundwater, respectively, with correlation coefficients marked next to the lines.

4 Discussion

4.1 Biodegradation Responsible for DOC Processing in Subsurface Environment

ΔDOC that represents DOC loss is estimated to evaluate to what extent DOM in HLGW is processed, based on the constraints of end-member analysis. Although glacier-snow and precipitation endmembers exhibit substantial uncertainties in their compositions (Table 2) due to altitudinal and temporal effects on isotopic compositions [*Chang et al.*, 2018; *Li et al.*, 2015], their effect on uncertainties of ΔDOC estimation is insignificant due to their low DOC content. In comparison, because the frozen soil endmember contains much more DOC than the glacier-snow and precipitation endmembers do, the uncertainty in ΔDOC estimation is mostly driven by the very small uncertainty of the soil endmember, and fortunately, is small (Table S1).

Both photodegradation and biodegradation can be important for mineralization of permafrost sourced DOC in high-altitude surface waters due to availability of sunlight [*Wang et al.*, 2018]. However, subsurface DOM is much less likely to undergo photo-oxidation or mineralization by sunlight, the DOC loss is therefore considered to mostly reflect biodegradation. The concurrent decreases of protein-like fluorophores and $SUVA_{254}$ with increasing DOC loss (Fig. 3) support the notion that aromatic DOM with high protein-like fluorophores, most likely

582 sourced from thawing of frozen soil, is subject to biodegradation in subsurface environment of
583 the HLGW. Further, the DOM quality changes in batch soil incubation support the utilization of
584 protein-like and aromatic C. While we cannot entirely rule out the possibility of photodegradation
585 due to frequent surface and subsurface water exchanges in HLGW, the transit time of subsurface
586 water should be longer than that of stream water, allowing for microbial processing time of DOM
587 in subsurface environment. The longer it takes for water to flow through subsurface, the higher
588 the DOC loss by microbial activities will be along this flow path. We take advantage of this
589 linkage to calculate MTT of groundwater using its ΔDOC obtained at the outlet of HLGW as
590 discussed in 4.2 next. The MTT reflects the flow pathways and water dynamics of the whole
591 system [*McGuire et al.*, 2005].

592

593 **4.2 Groundwater Mean Transit Time (MTT) in Response to Freeze-Thaw Cycles**

594 In the Arctic permafrost region, groundwater discharge is driven by soil freeze – thaw
595 processes with long water retention time [*Ameli et al.*, 2017; *Ireson et al.*, 2013; *Walvoord and*
596 *Striegl*, 2007] and horizontal flow path [*Aiken et al.*, 2014; *O'Donnell et al.*, 2012]. This longer
597 retention time explains the variable but usually low percentages of protein-like fluorophores:
598 0.3–22% in eight streams extending 250 km at Yenisei basin [*Kawahigashi et al.*, 2004]; 1–12%
599 over 500 km at Yukon basin and its small tributaries [*O'Donnell et al.*, 2010; *Wickland et al.*,
600 2012]. HLGW is small (25 km^2) and alpine (11° topographical gradient) so the groundwater
601 MTT is expected to be short though not previously quantified. Only a handful of studies have
602 attempted to quantify mean transit time in hillslopes. MTT of days to weeks (10 – 25 days) has
603 been obtained for storm events, based on hydrometric and isotopic tracer approach in an alpine
604 watershed of Oregon [*McGuire and McDonnell*, 2010]. Very short transit time of 2 to 12 days is
605 observed for a mountain spring in Hong Kong constrained by radium (Ra) and radon (Rn)
606 isotopes along a steep slope [*Luo and Jiao*, 2019].

607 In the following, we first discuss qualitative evidence for MTT of groundwater in HLGW
608 responding to the seasonal freeze-thaw cycles followed by an attempt to quantify the MTT in
609 low and high discharge periods.

610 First, DOC concentrations of groundwater and spring collected at the same locations
611 close to the outlet of HLGW reach a maximum in July during peak discharge, higher than those

in September when discharge is much less (Fig. 4). The ΔDOC of these subsurface waters are 1.0±0.1 mg L^{-1} in July and 2.5±0.4 mg L^{-1} in September, respectively, suggesting lower loss in July than in September. This contrast is neither attributable to a difference in DOC_0 (July: 3.2±0.04 mg L^{-1}; September: 3.2±0.2 mg L^{-1}) nor to water temperature (5 °C). It is unlikely due to adsorption alone because DOM adsorption is rapid, and usually reaches equilibrium within a few minutes to hours [*Gu et al.*, 1994; *Kalbitz and Wennrich*, 1998]. Further, retardation of DOM due to sorption only "delays" the arrival of influent DOC by 1.5 to 3 pore volumes in sandy to clayey columns [Li and Shuman, 1997]. Therefore, this retardation of DOC transport alone is unlikely to account for large changes in DOC concentrations at the outlet over 2 months (Fig. 4).

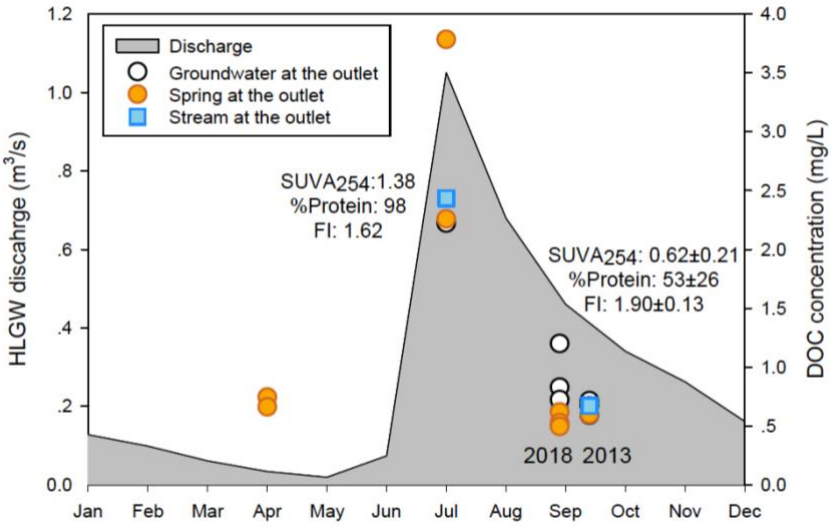

Figure 4. Monthly average stream discharge (left y-axis) in 2013 displayed in gray shade recorded at the gauging station (2960 m a.s.l) at the outlet of HLGW. Concentrations of DOC (right y-axis) in surface water (blue square) and springs (orange circles) and groundwater (white circles) from a monitoring well (MW – 30 m depth in Fig. 1d), all close to the gauging station, are higher in July than in September. Numbers are values of $SUVA_{254}$ (L mg C^{-1} m^{-1}), proportion of protein-like compound (%) and FI for groundwater from the MW.

Second, the protein-like proportion and $SUVA_{254}$ of all subsurface waters at the outlet are higher in July (98±0.5%, 1.25±0.41 L mg C^{-1} m^{-1}, n=3) and lower in September (45±23%, 0.66±0.26 L mg C^{-1} m^{-1}, n=10). The inferred shorter MTT in July allows for more DOM with stronger permafrost DOM fingerprint to be detected in the subsurface environment. This change is especially clear when groundwaters repeatedly sampled from a single monitoring well screened at 30 m depth below ground (MW, see Fig.1d) in July 2013, September 2013 and 2018

636 are considered (Fig. 4). Moreover, the DOC contrast in surface water is also consistent with this
637 difference in transit time (Fig. 4). The higher discharge and thus more extensive surface water
638 and groundwater interaction in July compared to September accelerates the already rapid
639 downward flow of groundwater in HLGW, also supported by field observation of the spring
640 discharge at the outlet of HLGW.

641 Third, an attempt is made to estimate groundwater MTT based on the DOC dynamics
642 described above, assuming subsurface biodegradation of DOC with first order kinetics (λ) that
643 is known to vary so the rationale for our choice is described. Incubation of 12 riverine DOM
644 samples yield λ from 0.147 to 0.781 d^{-1} in headwater regions of the Yangtze, Yellow and
645 Lantsang -Mekong rivers [*Ma et al*., 2018]. We adopt the average λ value of 0.25 d^{-1} from 2
646 riverine DOM samples in 2 small alpine watersheds (94.3304ºE, 35.75439º N) of the Yellow
647 River in Qinghai as the most likely for HLGW, given the similar topography, landscape (glacier
648 and permafrost), proximity (~ 500 km from HLGW), and comparable DOC concentration of
649 2.5±0.4 mg L^{-1} and discharge of 1.27 m^3/s [*Ma et al*., 2018]. The λ becomes 0.06 d^{-1} after
650 correcting to HLGW groundwater temperature of 5°C following the Arrhenius equation [*Catalan*
651 *et al.*, 2016]. Using 0.06 d^{-1}, the MTT is estimated to be approximately 6 days and 20 days in
652 July and September, respectively, corresponding to the changes in ΔDOC ($\Delta DOC/DOC_0$)
653 observed for groundwater of monitoring well at HLGW outlet of 32% in July and 74% in
654 September (Fig. 5). Because most DOC entered the aquatic environment in the upper stretch of
655 HLGW (Fig. 1), this estimation of reaction time based on DOC degradation is thus indicative of
656 MTT for groundwater in HLGW.

657 Fourth, the sensitivity of MTT estimate to variable λ is described as follows. The SOC
658 degradation constant of 0.32 d^{-1} established from our HLGW soil at 20ºC is within the range of
659 λ from the 12 riverine DOM sample. However, incubation studies of Arctic water DOM have
660 found variable λ of 5×10^{-3} to 0.15 d^{-1} [*Balcarczyk et al.*, 2009; *Fellman et al.*, 2008; *Fellman et*
661 *al.*, 2009; *Spencer et al.*, 2015]. The highest λ of 0.15 d^{-1} is established from the first-order
662 streams of the Kolyma River, most likely to be representative of highly labile and freshly released
663 DOC in Arctic headwaters [*Spencer et al.*, 2015], and thus relevant. The slowest λ of 5×10^{-3} d^{-1}
664 is reported for incubation of DOM in the stream waters from large basins with long retention
665 time and Holocene deposit in Alaska at 4ºC with in situ nutrients [*Balcarczyk et al.*, 2009].

Although these very long rates are unlikely, we have estimated the shortest and longest MTT using the faster λ_{SOC} and slowest λ. The λ_{SOC} becomes 0.11 d^{-1} at 5°C after temperature correction, and the MTT is estimated to be 3.5 d and 12.5 d for July and September, respectively (Fig. 5). Based on the slowest λ of 5×10^{-3} d^{-1} the MTT can be as long as 200 d for July and 700 d for September, respectively (Fig. 5).

There are several limitations to our MTT estimation. Given the degrees of spatial and temporal variability in DOM quantity and quality, biodegradation kinetics of DOM warrants further investigation. Perhaps more useful would be an independent assessment of groundwater MTT using Ra-Rn isotopes [*Luo and Jiao*, 2019]. Further, changes in DOC and $SUVA_{254}$ from our soil incubation experiments suggest release of aromatic carbon (Table S2). This raises the yet to be assessed possibility that preferential sorption of highly aromatic carbon or humic-like compounds onto soil or sediment may contribute to DOC loss along the groundwater flow path [*Jin and Zimmerman*, 2010]. Finally, long-term observations of DOM quantity and quality are desirable to reveal DOM dynamics that will allow separation of effects of gradual, seasonal freeze-thaw cycles and abrupt, accelerated thawing of permafrost. These limitations are unlikely to challenge the finding that subsurface DOM processing is primarily driven by biodegradation, and the rate constants are similar in July and September. If so, the results are interpreted to suggest that MTT in hillslopes vary in response to discharge corresponding to season freeze-thaw cycles.

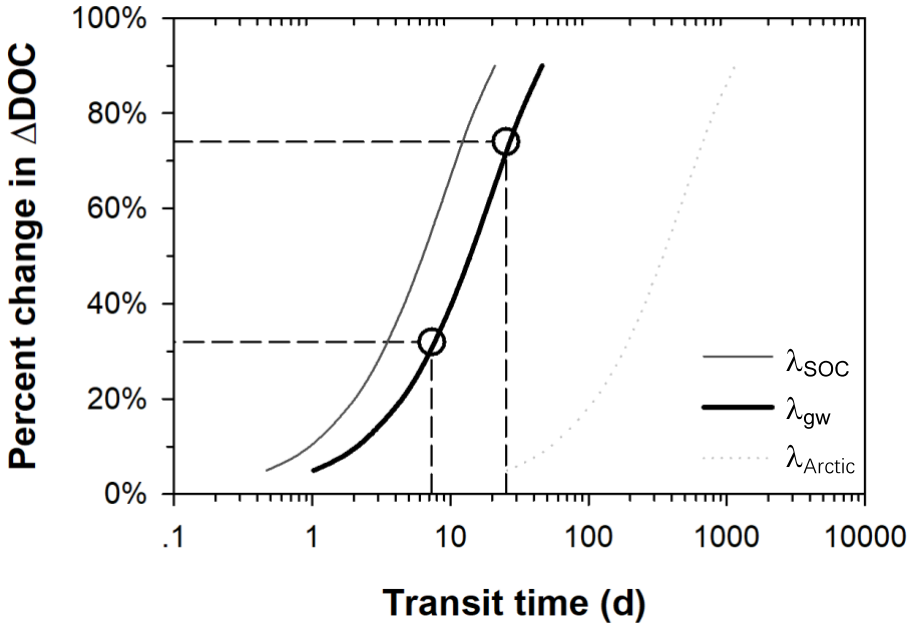

Figure 5. Percent changes in ΔDOC vs MTT (d) shown in log scale. Black line is for the most likely biodegradation rate constant (λ_{gw}) of 0.06 d^{-1}. The different groundwater MTT is shown as white circles to reflect percent changes in ΔDOC observed at MW in July (32%) and September (74%), respectively. The gray line to the left indicates a constant (λ_{SOC}) of 0.11 d^{-1} at 5°C based on HLGW soil incubation experiment. The dotted gray line (λ_{Arctic}) to the right indicates that MTT estimates using the lowest observed λ of 5×10^{-3} d^{-1} based on incubation of Arctic stream water samples [*Balcarczyk et al.*, 2009].

4.3 Hillslopes Act as Hotspots of Permafrost Derived DOC Processing in Subsurface Environment

Although better constraints on DOC degradation kinetics and repeated monthly sampling from June to December of groundwater would likely result in improved estimates of mean transit time in HLGW, the results nevertheless demonstrate that DOM in permafrost regions of the QTP can be used to shed light on hillslope hydrological process in its headwaters. A long-held view is that aquifer is dominated by water with older ages (> 3 months) compared to riverine systems of much younger water (< 3 months) [*Jasechko et al.*, 2017]. Recent studies suggest a component of groundwater is very young in age [*Gleeson et al.*, 2016], yet unraveling the age distribution is currently challenging with long-term tracer observations [*Luo and Jiao*, 2019; *McDonnell et al.*, 2010]. Though fraught with uncertainties, the estimation above is addressing a challenging

problem, and represents the first attempt to quantify hillslope groundwater transit time in the QTP. A global evaluation has shown that the DOC decomposition rate in inland waters ranges from 0.0003 to 9 d^{-1} corresponding to a water retention time of 0.04 day to 42 years [*Catalan et al.*, 2016]. This study supports the notion that hillslopes are hotspots for DOC processing with subsurface environment playing an important role, expanding the coverage of the aforementioned global evaluation to include an important inland water system in QTP.

Existing and newly gained insights on groundwater flow system in HLGW suggest extensive surface water and groundwater interaction, supported by modeling [*Evans et al.*, 2015], isotopic [*Ma et al.*, 2017], hydrochemical [*Li et al.*, 2014; *Li et al.*, 2016] and now DOM quantity and quality data. These studies have identified shallow groundwater sourced primarily from glacier-snow and precipitation [*Chang et al.*, 2018], and flows down gradient above permafrost layer and later above the clay layer (Fig. 1d) [*Evans et al.*, 2015; *Ma et al.*, 2017]. Hydrogeological studies have shown that the subsurface water's radiocarbon age is modern and contains tritium (^3H) at shallow depth (<20 m) in permafrost and seasonal frost zones of the HLGW [*Ma et al.*, 2017]. This understanding of groundwater flow together with its extensive interaction with surface water is taken as representative of headwater watersheds with permafrost of alpine hillslopes in the entire QTP. Considering the significantly lower DOC loss in July than that in September based on differences in ΔDOC, the DOC fluxes were estimated for July and other months, June to December except July. This assumes that September is representative of other months which have lower discharges (Fig. 4), and the input and export of water is mass balanced thus the same. Fluxes between January and May are not considered because the discharge is very low and the soil is frozen.

We put this all together to estimate DOC input and output fluxes to illustrate the extent of DOC loss in HLGW. In July, the DOC export is estimated to be 6.8×10^3 kg by multiplying monthly discharge and DOC concentration of 2.4 mg L^{-1} from the outlet stream water of HLGW (Table 4). We assume that the discharge of the HLGW outlet equals to the total of water recharge from the three end-members to meet the volume balance. We take the DOC mass of glacier-snow melting water as an example to present the estimation of DOC input. The input water volume is calculated as total discharge of 2.8×10^6 m^3 multiplying its contribution fraction of 23% in the outlet water sample. The input DOC mass of 0.3×10^3 kg is based on the DOC value in glacier

end member of 0.5 mg L^{-1}multiplying the water volume. Therefore, the DOC input flux is 8.4×10^3 kg, with the glacier-snow meltwater, precipitation, and soil meltwater contributing 0.3×10^3, $1.7\times10^3$and 6.4×10^3 kg, respectively (Table 4). Between June to December excluding July, the DOC concentration of 0.7 mg L^{-1} in September is representative for these months. The DOC export is 3.5×10^3 kg, and the DOC input is 15.1×10^3 kg with the glacier-snow meltwater, precipitation, and soil melt water contributing 0.6×10^3 kg, 3.1×10^3 kg and 11.4×10^3 kg, respectively (Table 4). The annual DOC input flux is 23.5×10^3 kg yr^{-1}, with an annual DOC export flux of 10.3×10^3 kg yr^{-1}. The difference between input and export DOC fluxes is taken to represent a "lost" DOC flux of 13.2×10^3 kg yr^{-1}within HLGW before transporting into large rivers (Fig. 1c and Table 4). About half of the DOC is processed in hillslopes of small alpine watersheds, comprising a substantial fraction in C cycling in permafrost region under warming and warrant further attention.

Table 4. Input, export and respired DOC fluxes from HLGW.

Input DOC from three endmembers							
End members	DOC (mg/L)	Fraction	July		June-Dec w/o July *		Annual flux (10^3 kg/yr)
			Water vol. (10^6 m^3)	DOC mass (10^3 kg)	Water vol. (10^6 m^3)	DOC mass (10^3 kg)	
G	0.5	23%	0.65	0.3	1.16	0.6	
P	1.0	62%	1.74	1.7	3.12	3.1	
S	15.0	15%	0.42	6.4	0.76	11.4	
Input DOC ($x10^3$ kg)				**8.4**		**15.1**	**23.5**
Export DOC at the outlet of HLGW							
Stream at outlet			July		June-Dec w/o July		Annual flux (10^3 kg/yr)
			DOC (mg/L)	Water vol. (10^6 m^3)	DOC mass (10^3 kg)	DOC (mg/L)	Water vol. (10^6 m^3)	DOC mass (10^3 kg)	
Export DOC ($x10^3$ kg)			2.4	2.8	**6.8**	0.7	5.0	**3.5**	**10.3**
Loss of DOC during in-stream processing							
			July			June-Dec w/o July		Annual
Loss of DOC (10^3 kg)					**1.6**			**11.6**	**13.2**
% lost DOC					19%			77%	56%

Input and output DOC between January and May are not considered due to seasonal freeze.

Acknowledgments and Data

We thank field team, Qixin Chang, Yalu Hu and Zhao Pan of CUG; Yu Xia, Chenyuan Dang and Ziqi Wu of SUSTech, and staff at the Qilian Station of CAS for their help with the fieldwork and for logistic assistance and quality time; Tom Strekas and Bob Engel of Queens College, CUNY for access to UV-Vis; Junjian Wang of SUSTech for access to TOC-L; Penghui Li and Zhen Tan for valuable discussion on PARAFAC. This study is supported by the National Natural Science Foundation (NSFC Grants No. 41772265, 41831279 and 41228003). All data are compiled and submitted in datasets S1 and S2 of supporting information, and will be archived in SUSTech open research data repository under Science Data Bank (http://www.dx.doi.org/10.11922/sciencedb.o00005.00007). We thank the editor and two anonymous reviewers for their constructive comments.

Reference

Aiken, G. R., R. G. M. Spencer, R. G. Striegl, P. F. Schuster, and P. A. Raymond (2014), Influences of glacier melt and permafrost thaw on the age of dissolved organic carbon in the Yukon River basin, Global Biogeochemical Cycles, 28(5), 525-537.

Ameli, A. A., K. Beven, M. Erlandsson, I. F. Creed, J. J. McDonnell, and K. Bishop (2017), Primary weathering rates, water transit times, and concentration-discharge relations: A theoretical analysis for the critical zone, Water Resources Research, 53(1), 942-960.

Balcarczyk, K. L., J. B. Jones, R. Jaffé, and N. Maie (2009), Stream dissolved organic matter bioavailability and composition in watersheds underlain with discontinuous permafrost, Biogeochemistry, 94(3), 255-270.

Barnes, R. T., D. E. Butman, H. F. Wilson, and P. A. Raymond (2018), Riverine Export of Aged Carbon Driven by Flow Path Depth and Residence Time, Environmental Science & Technology, 52(3), 1028-1035.

Benettin, P., J. W. Kirchner, A. Rinaldo, and G. Botter (2015), Modeling chloride transport using travel time distributions at Plynlimon, Wales, Water Resources Research, 51(5), 3259-3276.

Brogi, S. R., S.-Y. Ha, K. Kim, M. Derrien, Y. K. Lee, and J. Hur (2018), Optical and molecular characterization of dissolved organic matter (DOM) in the Arctic ice core and the underlying seawater (Cambridge Bay, Canada): Implication for increased autochthonous DOM during ice melting, Science of the Total Environment, 627, 802-811.

Catala, T. S., et al. (2015), Turnover time of fluorescent dissolved organic matter in the dark global ocean, Nature Communications, 6.

Catalan, N., R. Marce, D. N. Kothawala, and L. J. Tranvik (2016), Organic carbon decomposition rates controlled by water retention time across inland waters, Nature Geoscience, 9(7), 501-+.

Chang, Q., R. Ma, Z. Sun, A. Zhou, Y. Hu, and Y. Liu (2018), Using Isotopic and Geochemical Tracers to Determine the Contribution of Glacier-Snow Meltwater to Streamflow in a Partly Glacierized Alpine-Gorge Catchment in Northeastern Qinghai-Tibet Plateau, Journal of Geophysical Research-Atmospheres, 123(18), 10037-10056.

Cheng, G., and T. Wu (2007), Responses of permafrost to climate change and their environmental significance, Qinghai-Tibet Plateau, Journal of Geophysical Research, 112(F2).

Coble, P. G. (1996), Characterization of marine and terrestrial DOM in seawater using excitation emission matrix spectroscopy, Marine Chemistry, 51(4), 325-346.

Connolly, C. T., M. B. Cardenas, G. A. Burkart, R. G. M. Spencer, and J. W. McClelland (2020), Groundwater as a major source of dissolved organic matter to Arctic coastal waters, Nature Communications, 11(1).

Cory, R. M., and D. M. McKnight (2005), Fluorescence Spectroscopy Reveals Ubiquitous Presence of Oxidized and Reduced Quinones in Dissolved Organic Matter, Environmental Science & Technology, 39(21), 8142-8149.

Drake, T. W., P. A. Raymond, and R. G. M. Spencer (2018), Terrestrial carbon inputs to inland waters: A current synthesis of estimates and uncertainty, Limnology and Oceanography Letters, 3(3), 132-142.

Drake, T. W., K. P. Wickland, R. G. M. Spencer, D. M. McKnight, and R. G. Striegl (2015), Ancient low–molecular-weight organic acids in permafrost fuel rapid carbon dioxide production upon thaw, PROCEEDINGS OF THE NATIONAL ACADEMY OF SCIENCES.

Evans, S. G., S. Ge, and S. Liang (2015), Analysis of groundwater flow in mountainous, headwater catchments with permafrost, Water Resources Research, 51(12), 9564-9576.

Fellman, J. B., D. V. D'Amore, E. Hood, and R. D. Boone (2008), Fluorescence characteristics and biodegradability of dissolved organic matter in forest and wetland soils from coastal temperate watersheds in southeast Alaska, Biogeochemistry, 88(2), 169-184.

Fellman, J. B., E. Hood, R. T. Edwards, and D. V. D'Amore (2009), Changes in the concentration, biodegradability, and fluorescent properties of dissolved organic matter during stormflows in coastal temperate watersheds, Journal of Geophysical Research-Biogeosciences, 114.

Feng, L., J. Xu, S. Kang, X. Li, Y. Li, B. Jiang, and Q. Shi (2016), Chemical Composition of Microbe-Derived Dissolved Organic Matter in Cryoconite in Tibetan Plateau Glaciers: Insights from Fourier Transform Ion Cyclotron Resonance Mass Spectrometry Analysis, Environmental Science & Technology, 50(24), 13215-13223.

Frey, K. E., and J. W. McClelland (2009), Impacts of permafrost degradation on arctic river biogeochemistry, Hydrological Processes, 23(1), 169-182.
Froehlich, K., M. Kralik, W. Papesch, D. Rank, H. Scheifinger, and W. Stichler (2008), Deuterium excess in precipitation of Alpine regions - moisture recycling, Isotopes in Environmental and Health Studies, 44(1), 61-70.
Ge, S., J. McKenzie, C. Voss, and Q. Wu (2011), Exchange of groundwater and surface-water mediated by permafrost response to seasonal and long term air temperature variation, Geophysical Research Letters, 38.
Genereux, D. (1998), Quantifying uncertainty in tracer-based hydrograph separations, Water Resources Research, 34(4), 915-919.
Gleeson, T., K. M. Befus, S. Jasechko, E. Luijendijk, and M. B. Cardenas (2016), The global volume and distribution of modern groundwater, Nature Geoscience, 9(2), 161-+.
Gonçalvesaraujo, R., M. A. Granskog, A. Bracher, K. Azetsuscott, P. A. Dodd, and C. A. Stedmon (2016), Using fluorescent dissolved organic matter to trace and distinguish the origin of Arctic surface waters, Scientific Reports, 6(33978), 33978.
Green, S. A., and N. V. Blough (1994), Optical absorption and fluorescence properties of chromophoric dissolved organic matter in natural waters, Limnology and Oceanography, 39(8), 1903-1916.
Gu, B. H., J. Schmitt, Z. H. Chen, L. Y. Liang, and J. F. McCarthy (1994), ADSORPTION AND DESORPTION OF NATURAL ORGANIC-MATTER ON IRON-OXIDE - MECHANISMS AND MODELS, Environmental Science & Technology, 28(1), 38-46.
Guo, L., and R. W. Macdonald (2006), Source and transport of terrigenous organic matter in the upper Yukon River: Evidence from isotope (δ13C, Δ14C, and δ15N) composition of dissolved, colloidal, and particulate phases, Global Biogeochemical Cycles, 20(2).
Guo, L., C.-L. Ping, and R. W. Macdonald (2007), Mobilization pathways of organic carbon from permafrost to arctic rivers in a changing climate, Geophysical Research Letters, 34(13), n/a-n/a.
Heslop, J. K., M. Winkel, K. M. Walter Anthony, R. G. M. Spencer, D. C. Podgorski, P. Zito, A. Kholodov, M. Zhang, and S. Liebner (2019), Increasing Organic Carbon Biolability With Depth in Yedoma Permafrost: Ramifications for Future Climate Change, Journal of Geophysical Research: Biogeosciences, 124(7), 2021-2038.
Hu, Y., R. Ma, Y. Wang, Q. Chang, S. Wang, M. Ge, J. Bu, and Z. Sun (2019), Using hydrogeochemical data to trace groundwater flow paths in a cold alpine catchment, Hydrological Processes.
Ireson, A. M., G. van der Kamp, G. Ferguson, U. Nachshon, and H. S. Wheater (2013), Hydrogeological processes in seasonally frozen northern latitudes: understanding, gaps and challenges, Hydrogeology Journal, 21(1), 53-66.
Jasechko, S., et al. (2017), Global aquifers dominated by fossil groundwaters but wells vulnerable to modern contamination, Nature Geoscience, 10(6), 425-+.
Jin, J., and A. R. Zimmerman (2010), Abiotic interactions of natural dissolved organic matter and carbonate aquifer rock, Applied Geochemistry, 25(3), 472-484.
Kalbitz, K., and R. Wennrich (1998), Mobilization of heavy metals and arsenic in polluted wetland soils and its dependence on dissolved organic matter, Science of the Total Environment, 209(1), 27-39.
Kawahigashi, M., K. Kaiser, K. Kalbitz, A. Rodionov, and G. Guggenberger (2004), Dissolved organic matter in small streams along a gradient from discontinuous to continuous permafrost, Global Change Biology, 10(9), 1576-1586.
Li, C., F. Yan, S. Kang, P. Chen, Z. Hu, X. Han, G. Zhang, S. Gao, B. Qu, and M. Sillanpaa (2017), Deposition and light absorption characteristics of precipitation dissolved organic carbon (DOC) at three remote stations in the Himalayas and Tibetan Plateau, China, Science of the Total Environment, 605, 1039-1046.
Li, C., et al. (2018), Fossil Fuel Combustion Emission From South Asia Influences Precipitation Dissolved Organic Carbon Reaching the Remote Tibetan Plateau: Isotopic and Molecular Evidence, Journal of Geophysical Research-Atmospheres, 123(11), 6248-6258.
Li, Z., F. Qi, Q. J. Wang, Y. Song, L. Hongyi, and L. Yongge (2016), The influence from the shrinking cryosphere and strengthening evopotranspiration on hydrologic process in a cold basin, Qilian Mountains, Global and Planetary Change, 144, 119-128.

Li, Z., F. Qi, L. Wei, W. Tingting, C. Aifang, G. Yan, G. Xiaoyan, P. Yanhui, L. Jianguo, and G. Rui (2014), Study on the contribution of cryosphere to runoff in the cold alpine basin: A case study of Hulugou River Basin in the Qilian Mountains, Global and Planetary Change, 122, 345-361.

Li, Z., et al. (2015), The stable isotope evolution in Shiyi glacier system during the ablation period in the north of Tibetan Plateau, China, Quaternary International, 380, 262-271.

Li, Z. B., and L. M. Shuman (1997), Estimation of retardation factor of dissolved organic carbon in sandy soils using batch experiments, Geoderma, 78(3-4), 197-206.

Luo, X., and J. J. Jiao (2019), Unraveling controlling factors of concentration discharge relationships in a fractured aquifer dominant spring-shed: Evidence from mean transit time and radium reactive transport model, Journal of Hydrology, 571, 528-544.

Ma, R., Z. Sun, Y. Hu, Q. Chang, S. Wang, W. Xing, and M. Ge (2017), Hydrological connectivity from glaciers to rivers in the Qinghai-Tibet Plateau: roles of suprapermafrost and subpermafrost groundwater, Hydrology and Earth System Sciences, 21(9), 4803-4823.

Ma, X., G. Liu, X. Wu, H. Xu, L. Ye, X. Zhang , W. ai (2018), Bioavailability of Dissolved Organic Carbon in Rivers for Typical Vegetation Types in the Permafrost Regions on the Qinghai-Tibet Plateau, Environmental Science, 39(5), 2086-2094. Doi 10.13227/j.hjkx.201709280. (in Chinese)

Mann, P. J., T. I. Eglinton, C. P. McIntyre, N. Zimov, A. Davydova, J. E. Vonk, R. M. Holmes, and R. G. M. Spencer (2015), Utilization of ancient permafrost carbon in headwaters of Arctic fluvial networks, Nature Communications, 6.

McDonnell, J. J., et al. (2010), How old is streamwater? Open questions in catchment transit time conceptualization, modelling and analysis, Hydrological Processes, 24(12), 1745-1754.

McGuire, A. D., L. G. Anderson, T. R. Christensen, S. Dallimore, L. Guo, D. J. Hayes, M. Heimann, T. D. Lorenson, R. W. Macdonald, and N. Roulet (2009), Sensitivity of the carbon cycle in the Arctic to climate change, Ecological Monographs, 79(4), 523-555.

McGuire, A. D., et al. (2018), Dependence of the evolution of carbon dynamics in the northern permafrost region on the trajectory of climate change, Proceedings of the National Academy of Sciences of the United States of America, 115(15), 3882-3887.

McGuire, K. J., and J. J. McDonnell (2010), Hydrological connectivity of hillslopes and streams: Characteristic time scales and nonlinearities, Water Resources Research, 46.

McGuire, K. J., J. J. McDonnell, M. Weiler, C. Kendall, B. L. McGlynn, J. M. Welker, and J. Seibert (2005), The role of topography on catchment-scale water residence time, Water Resources Research, 41(5).

McKnight, D. M., E. W. Boyer, P. K. Westerhoff, P. T. Doran, T. Kulbe, and D. T. Andersen (2001), Spectrofluorometric characterization of dissolved organic matter for indication of precursor organic material and aromaticity, Limnology and Oceanography, 46(1), 38-48.

Murphy, K. R., C. A. Stedmon, D. T. Waite, and G. M. Ruiz (2008), Distinguishing between terrestrial and autochthonous organic matter sources in marine environments using fluorescence spectroscopy, Marine Chemistry, 108(1-2), 40-58.

Murphy, K. R., C. A. Stedmon, D. Graeber, and R. Bro (2013), Fluorescence spectroscopy and multi-way techniques. PARAFAC, Anal. Methods, 5(23), 6557-6566.

Murphy, K. R., C. A. Stedmon, P. Wenig, and R. Bro (2014), OpenFluor- an online spectral library of auto-fluorescence by organic compounds in the environment, Anal. Methods, 6(3), 658-661.

Neff, J. C., J. C. Finlay, S. A. Zimov, S. P. Davydov, J. J. Carrasco, E. A. G. Schuur, and A. I. Davydova (2006), Seasonal changes in the age and structure of dissolved organic carbon in Siberian rivers and streams, Geophysical Research Letters, 33(23).

O'Donnell, J. A., G. R. Aiken, E. S. Kane, and J. B. Jones (2010), Source water controls on the character and origin of dissolved organic matter in streams of the Yukon River basin, Alaska, Journal of Geophysical Research, 115(G3).

O'Donnell, J. A., G. R. Aiken, M. A. Walvoord, and K. D. Butler (2012), Dissolved organic matter composition of winter flow in the Yukon River basin: Implications of permafrost thaw and increased groundwater discharge, Global Biogeochemical Cycles, 26.

Parlanti, E., K. Wörz, L. Geoffroy, and M. Lamotte (2000), Dissolved organic matter fluorescence spectroscopy as a tool to estimate biological activity in a coastal zone submitted to anthropogenic inputs, Organic Geochemistry, 31(12), 1765-1781.

Plaza, C., et al. (2019), Direct observation of permafrost degradation and rapid soil carbon loss in tundra, Nature Geoscience, 12(8), 627-631.
Raymond, P. A., and R. G. M. Spencer (2015), Riverine DOM, 509,525-533 pp.
Raymond, P. A., et al. (2013), Global carbon dioxide emissions from inland waters, Nature, 503(7476), 355-359.
Spencer, R. G. M., W. Guo, P. A. Raymond, T. Dittmar, E. Hood, J. Fellman, and A. Stubbins (2014), Source and biolability of ancient dissolved organic matter in glacier and lake ecosystems on the Tibetan Plateau, Geochimica et Cosmochimica Acta, 142, 64-74.
Spencer, R. G. M., P. J. Mann, T. Dittmar, T. I. Eglinton, C. McIntyre, R. M. Holmes, N. Zimov, and A. Stubbins (2015), Detecting the signature of permafrost thaw in Arctic rivers, Geophysical Research Letters, 42(8), 2830-2835.
Stedmon, C. A., and R. Bro (2008), Characterizing dissolved organic matter fluorescence with parallel factor analysis: a tutorial, Limnology and Oceanography-methods, 6(11), 572-579.
Stedmon, C. A., D. N. Thomas, S. Papadimitriou, M. A. Granskog, and G. S. Dieckmann (2011), Using fluorescence to characterize dissolved organic matter in Antarctic sea ice brines, Journal of Geophysical Research-Biogeosciences, 116.
Striegl, R. G., G. R. Aiken, M. M. Dornblaser, P. A. Raymond, and K. P. Wickland (2005), A decrease in discharge-normalized DOC export by the Yukon River during summer through autumn, Geophysical Research Letters, 32(21).
Tarnocai, C., J. G. Canadell, E. A. G. Schuur, P. Kuhry, G. Mazhitova, and S. Zimov (2009), Soil organic carbon pools in the northern circumpolar permafrost region, Global Biogeochemical Cycles, 23.
Turetsky, M. R., et al. (2020), Carbon release through abrupt permafrost thaw, Nature Geoscience, 13(2), 138-143.
Vonk, J., S. Tank, and M. Walvoord (2019), Integrating hydrology and biogeochemistry across frozen landscapes, Nature Communications, 10.
Vonk, J. E., et al. (2013), High biolability of ancient permafrost carbon upon thaw, Geophysical Research Letters, 40(11), 2689-2693.
Walvoord, M. A., and R. G. Striegl (2007), Increased groundwater to stream discharge from permafrost thawing in the Yukon River basin: Potential impacts on lateral export of carbon and nitrogen, Geophysical Research Letters, 34(12).
Wang, T., D. Yang, Y. Yang, S. Piao, X. Li, G. Cheng, and B. Fu (2020), Permafrost thawing puts the frozen carbon at risk over the Tibetan Plateau, Science Advances, 6(19).
Wang, Y., R. G. M. Spencer, D. C. Podgorski, A. M. Kellerman, H. Rashid, P. Zito, W. Xiao, D. Wei, Y. Yang, and Y. Xu (2018), Spatiotemporal transformation of dissolved organic matter along an alpine stream flow path on the Qinghai-Tibet Plateau: importance of source and permafrost degradation, Biogeosciences, 15(21), 6637-6648.
Ward, C. P., and R. M. Cory (2016), Complete and Partial Photo-oxidation of Dissolved Organic Matter Draining Permafrost Soils, Environmental Science & Technology, 50(7), 3545-3553.
Weishaar, J. L., G. R. Aiken, B. A. Bergamaschi, M. S. Fram, R. Fujii, and K. Mopper (2003), Evaluation of specific ultraviolet absorbance as an indicator of the chemical composition and reactivity of dissolved organic carbon, Environmental Science & Technology, 37(20), 4702-4708.
Wickland, K. P., G. R. Aiken, K. Butler, M. M. Dornblaser, R. G. M. Spencer, and R. G. Striegl (2012), Biodegradability of dissolved organic carbon in the Yukon River and its tributaries: Seasonality and importance of inorganic nitrogen, Global Biogeochemical Cycles, 26(4).
Wunsch, U. J., J. K. Geuer, O. J. Lechtenfeld, B. P. Koch, K. R. Murphy, and C. A. Stedmon (2018), Quantifying the impact of solid-phase extraction on chromophoric dissolved organic matter composition, Marine Chemistry, 207, 33-41.
Xu, J., Q. Zhang, X. Li, X. Ge, C. Xiao, J. Ren, and D. Qin (2013), Dissolved Organic Matter and Inorganic Ions in a Central Himalayan Glacier-Insights into Chemical Composition and Atmospheric Sources, Environmental Science & Technology, 47(12), 6181-6188.
Yang, M., F. E. Nelson, N. I. Shiklomanov, D. Guo, and G. Wan (2010), Permafrost degradation and its environmental effects on the Tibetan Plateau: A review of recent research, Earth-Science Reviews, 103(1-2), 31-44.

973 Yao, Y., C. Zheng, C. Andrews, Y. Zheng, A. Zhang, and J. Liu (2017), What controls the partitioning between
974 baseflow and mountain block recharge in the Qinghai-Tibet Plateau?, *Geophysical Research Letters*,
975 *44*(16), 8352-8358.
976 Yi, S., Q. Wang, and W. Sun (2016), Basin mass dynamic changes in China from GRACE based on a
977 multibasin inversion method, Journal of Geophysical Research-Solid Earth, 121(5), 3782-3803.
978 Zhang, G., et al. (2017), Lake volume and groundwater storage variations in Tibetan Plateau's endorheic basin,
979 Geophysical Research Letters, 44(11), 5550-5560.
980 Zhang, X., J. A. Hutchings, T. S. Bianchi, Y. Liu, A. R. Arellano, and E. A. G. Schuur (2017), Importance of
981 lateral flux and its percolation depth on organic carbon export in Arctic tundra soil: Implications from a
982 soil leaching experiment, 122(4), 796-810.

[JGR Biogeosciences]

Supporting Information for

[Hillslopes in Headwaters of Qinghai-Tibetan Plateau as Hotspots for Subsurface Dissolved Organic Carbon Processing during Permafrost Thaw]

[Yuqin Sun[1,2,3], Kale Clauson[4], Min Zhou[1], Ziyong Sun[5], Chunmiao Zheng[2,3] and Yan Zheng[2,3*]]

[[1] College of Engineering, Peking University, Beijing, 100871, China.

[2] State Environmental Protection Key Laboratory of Integrated Surface Water-Groundwater Pollution Control, School of Environmental Science and Engineering, Southern University of Science and Technology, Shenzhen, 518055, China.

[3] Guangdong Provincial Key Laboratory of Soil and Groundwater Pollution Control, School of Environmental Science and Engineering, Southern University of Science and Technology, Shenzhen, 518055, China.

[4] School of Earth and Environmental Sciences, Queens College, City University of New York, Flushing, NY 11367, USA.

[5] School of Environmental Studies, China University of Geosciences, Wuhan 430074, China.]

Contents of this file

Additional Supporting Information (Files uploaded separately)

Introduction

Supporting information contains descriptions of sampling protocols, field and laboratory measurement details (Text S1), soil incubation experimental procedure (Text S2) and results (Text S3). Figures S1 and S6 illustrates the variations of $SUVA_{254}$ FI and BIX. Figure S2 depicts the soil incubation experiment set up. Figures S3 – S5 show fluorescent characteristics of the DOM samples and PARAFAC modeling results. Tables S1 reports uncertainties of endmember compositions and analysis. Table S3 and Figure S7 report soil incubation experimental data. Dataset S1 to S2 (separate electronic files) are original data of field and laboratory measurements of water chemistry parameters for all samples.

Text S1. Sampling and Measurements.

Temperature (T), electrical conductivity (EC) and pH were measured in the field using WTW-COND-3301 instrument in 2012 and 2013, and Thermo 520M-01A instrument in 2018. Alkalinity was measured using titration method in the field [*Gran*, 1952]. All samples were stored on ice at 4°C for shipment to laboratory.

Stable isotopes (δD and δ^{18}O) were measured for samples collected in July 2013, and September of 2013 and 2018 on a water isotope spectrometer analyzer (Model PICARRO L2130-I) at Pri-ecoco, Beijing, China. Three standard solutions (GBW58, GBW59, and GBW60) were employed as daily QA/QC. Each sample was analyzed 6 times and the result was calculated as the average of the last three injections. The relative standard deviation (RSD) for duplicate analysis was < 0.8%. The isotope compositions are expressed as the δ-notation related to Vienna Standard Mean Ocean Water (VSMOW) in ‰.

DOC concentrations for samples collected in 2012 and 2013 were measured on a TOC-5000 Analyzer (Shimadzu) at both the Environmental Engineering Laboratory, Peking University and Queens College, CUNY according to a Non Purgeable Organic Carbon (NPOC) method. Samples collected in 2018 were analyzed by a TOC-L Analyzer (Shimadzu) at Southern University of Science and Technology following the same protocol. Samples were analyzed in triplicate with the RSD less than 3% as a threshold for accepting the result.

Measurement of cations was performed using Inductively Coupled Plasma Atomic Emission Spectrometry (ICP-AES) at Peking University for samples collected in 2012 and 2013. Anions of nitrate (NO_3), sulfate (SO_4) and chloride (Cl) were measured using ion chromatography (IC) at Peking University. Major anions and cations concentrations were measured using IC at Southern University of Science and Technology for samples collected in 2018.

Text S2. Experimental Procedure of Soil Incubation.

At the start of the second incubation in the reactor, 100 g of wet soil was weighed and added to a glass reactor and filled with 5L CO_2-free MQ water without headspace at room temperature. The reactor was kept in dark for 80 hours, with a peristaltic pump running at 29 ml/min to ensure mixing. The inlet and outlet of the reactor were connected with 6M NaOH solution to maintain CO_2-free headspace (Fig. S1). A total of 29 samples were collected at an interval of 30 min in the initial 4.6 hours, at an interval of 60 min till 12 hours, and at an interval of 180 min until the end of incubation that lasted 80 hours. At each sampling time, approximately 75 ml of water was removed. Water volume and pH were measured immediately before filtering with 0.22 µm SPE filters. Filtered samples were analyzed for DOC concentrations, UV-vis and fluorescence as in section 2.2 of the main text.

Text S3. Soil Incubation Results.

During the 80-hours dark incubation of the frost soil in the reactor, the carbon mass of DOC decreases from 30 mg to 12 mg in the initial 12 hours (Fig. S6a). The utilization of aromatic DOC is supported by the doubling of $SUVA_{254}$ values concurrent with a 60% decrease in DOC mass in the system between 0 to 12 hours (Fig. S6). From 12 hours to 80 hours, $SUVA_{254}$ values instead decreased with an increase of DOC mass from 12 mg to 18 mg (Fig. S6c). The EEMs of all incubation samples show the main fluorescent peak at excitation of 230 nm and emission of 240 nm, suggesting that protein-like fluorophores are significant.

The first-order kinetic equation was applied to fit the SOC degradation curves for the decrease in DOC mass in the first 12 hrs (Fig. S6c). The half-time of soil derived DOC degradation is estimated to be 5 hours, and the degradation constant is calculated as dividing -ln (0.5) by half-time. Therefore, the degradation constant following first-order kinetics of DOC derived from permafrost soil is estimated to be 0.32 d^{-1} at 20^{o}C, and is corrected to 0.11 d^{-1} for 5^{o}C.

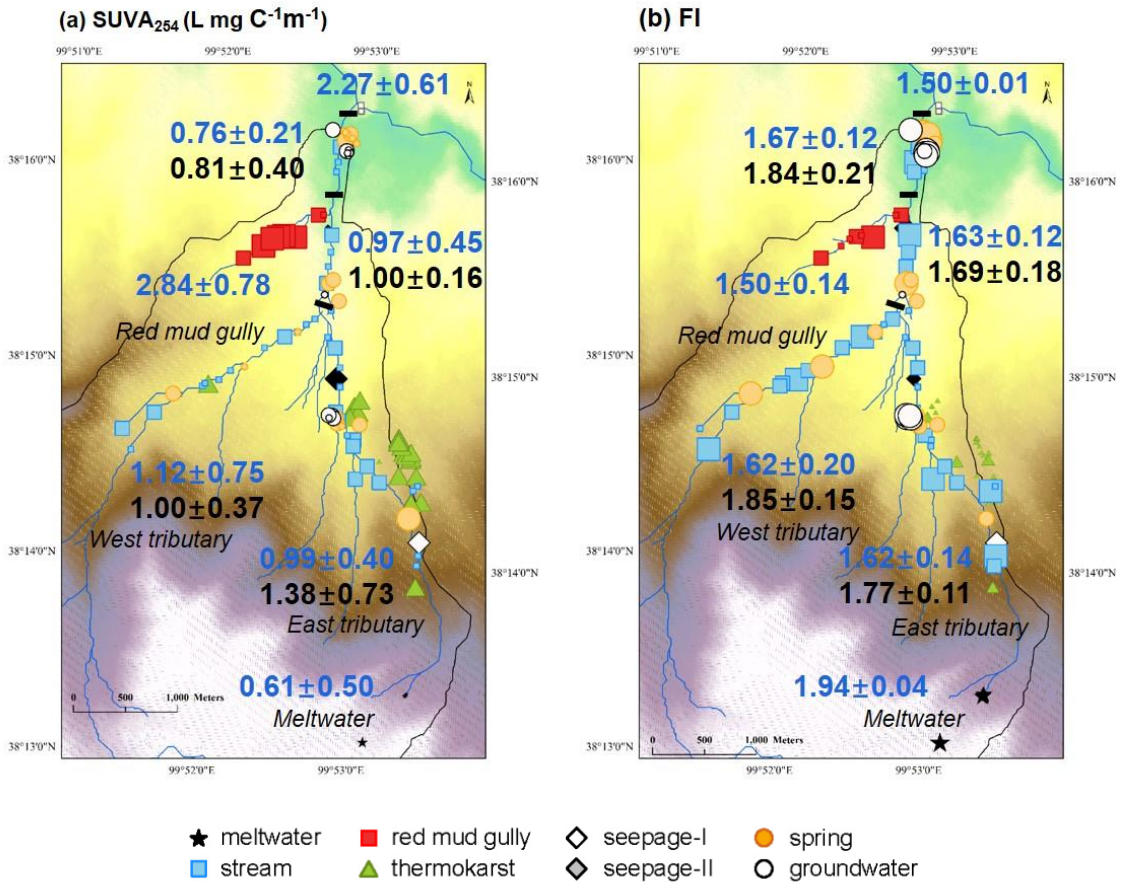

Figure S1. (a) $SUVA_{254}$ for eight types of water in HLGW, Qinghai-Tibetan Plateau. Small, medium and large symbol sizes indicate low (< 0.91 L mg C^{-1} m^{-1}), medium (0.91–2.46 L mg C^{-1} m^{-1}) and high (>2.46 L mg C^{-1} m^{-1}) $SUVA_{254}$ according to tertile values of the entire dataset. Numbers are mean value ± one standard deviation for $SUVA_{254}$ in stream (blue) and subsurface water (black). (b) FI with small, medium and large symbol sizes indicate low (<1.59), medium (1.59–1.69) and high (>1.69) according to tertile values. Numbers are mean value ± one standard deviation for FI in stream (blue) and subsurface water (black).

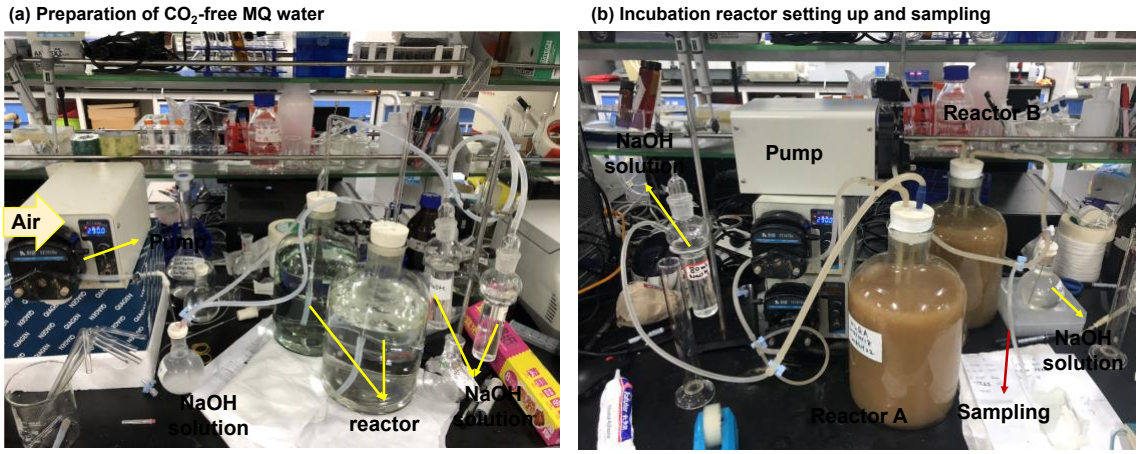

Figure S2. Figure S1. Experimental set up of frost soil reactor incubation. Left photo shows the preparation of CO_2-free water for the two reactors. Right photo shows ongoing experiment with sampling port location during incubation. The reactors used 5-L glass containers with inlet and outlet ports. Continuous mixing is ensured by pumping water at a rate of 29 mL min^{-1} from the reactors by a peristaltic pump through a CO2-free chamber. Samples were collected by a syringe at the sampling port with a three-way valve.

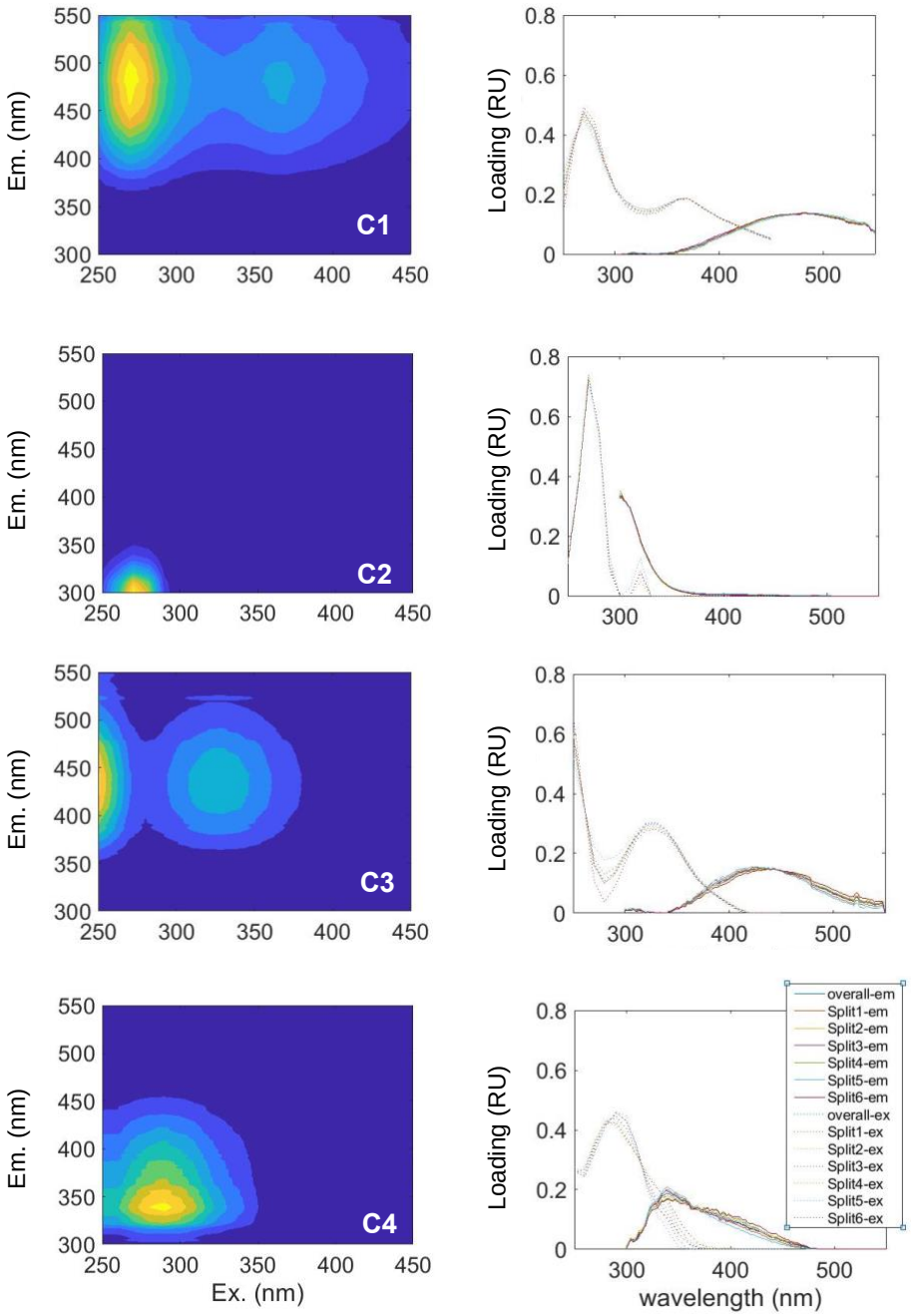

Figure S3. Fluorescence matrixes of the four identified components (left) and loadings of excitation (the dot lines) and emission (the solid lines) wavelength (right), respectively. Component 1 (ex: 270/370 nm, em: 470 nm) and component 3 (ex: <250/330 nm, em:420 nm) represent two humic-like components. Fluorescence characteristic of C2 (ex: 270 nm, em: 304 nm) represents tyrosine-like material [*D'Andrilli et al.*, 2019] (20), and C4 (ex: 290 nm, em: 338 nm) represents amino-acids, free or bound in proteins compounds [*Catala et al.*, 2015; *Murphy et al.*, 2008].

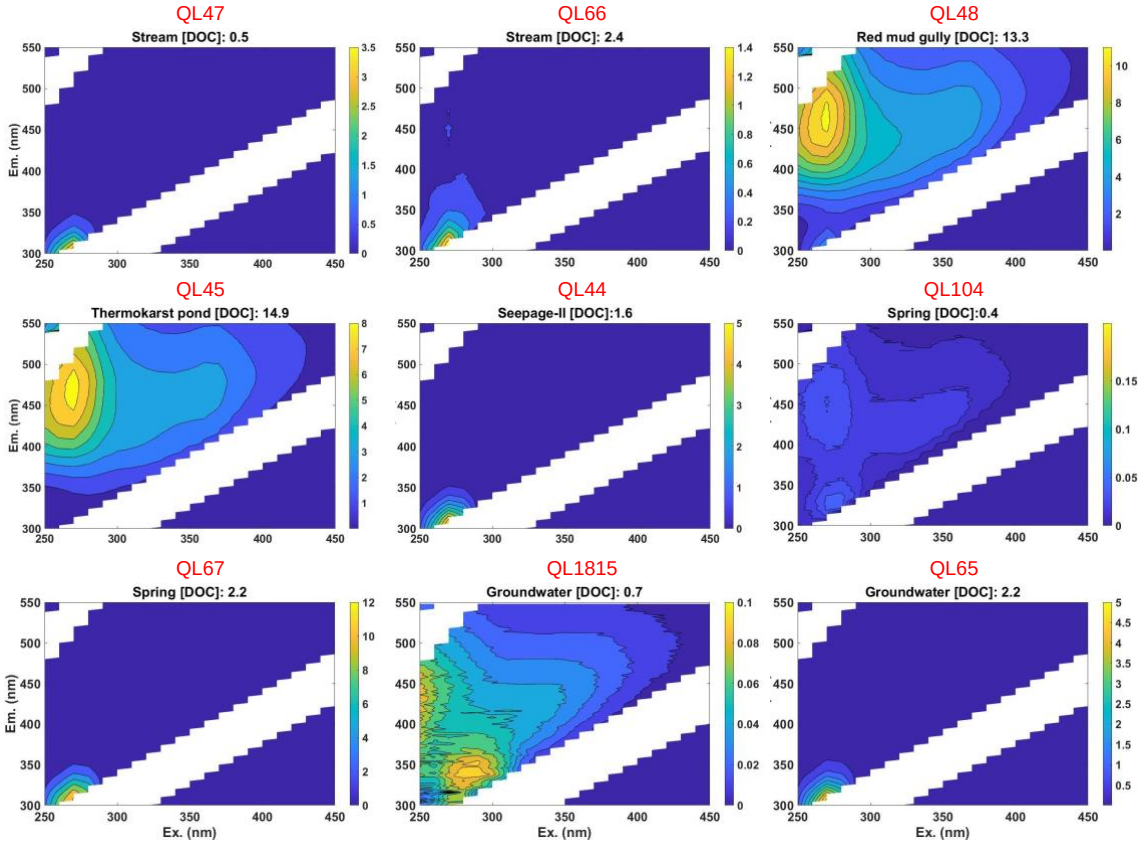

Figure S4. EEMs plots of typical stream, red mud gully, thermokarst pond, seepage-II, spring and groundwater samples in HLGW. Sample ID is written in red (see Data set S1 for details), and the DOC concentration (mg L^{-1}) is written in black above each EEMs. Color bar represents the fluorescence intensity.

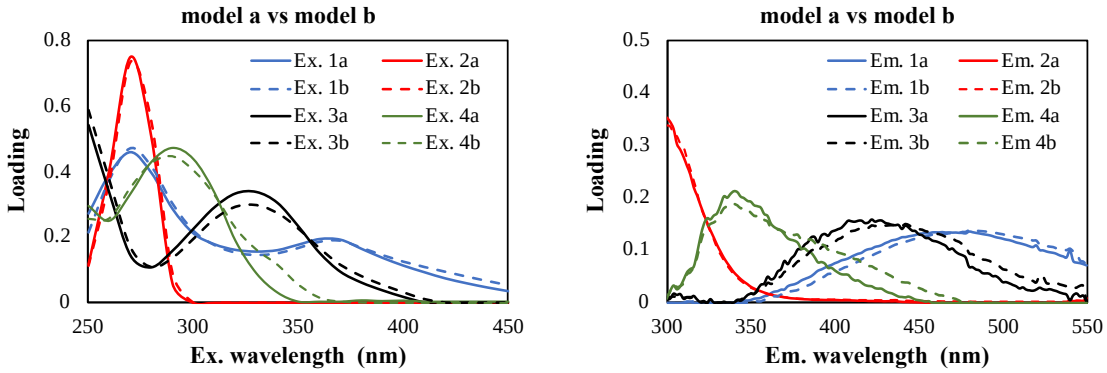

Figure S5. Comparison of excitation (Ex.) and emission (Em.) loadings of the four-components models.

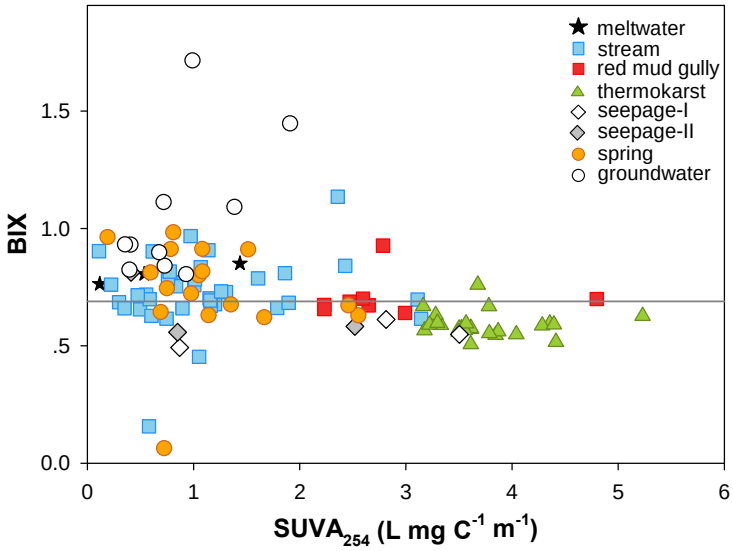

Figure S6. $SUVA_{254}$ vs BIX for eight types of water samples with gray line indicating the median value of BIX for entire dataset.

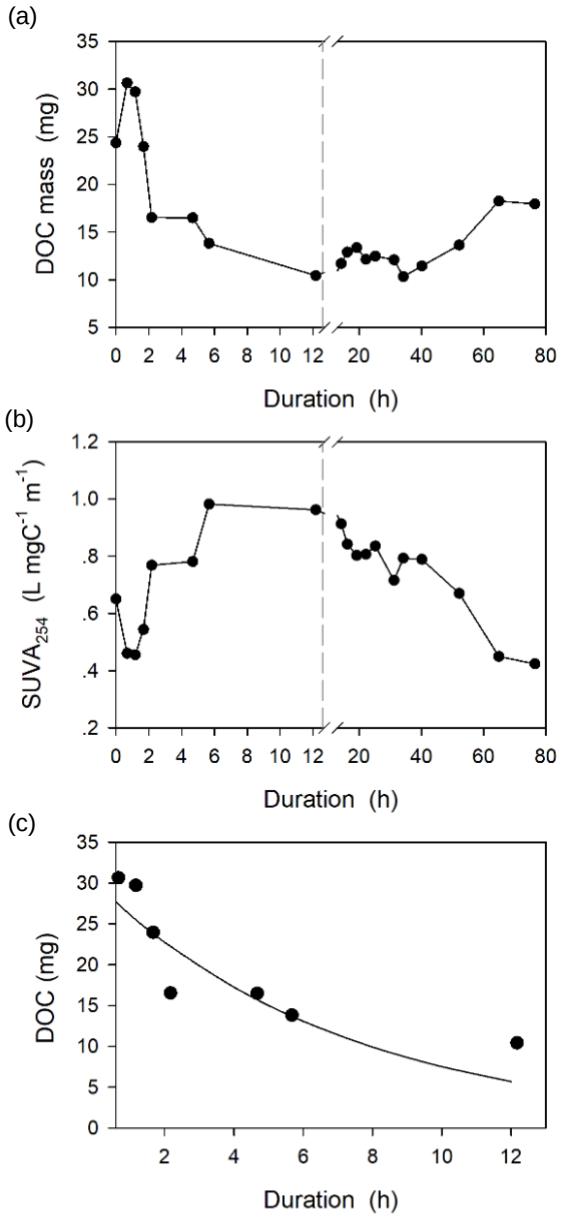

Figure S7. Changes of (a) DOC expressed as carbon mass in supernatant and (b) $SUVA_{254}$ values over 80 hrs for the reactor soil incubation experiment in dark. The first-order kinetics fit to the soil carbon derived DOC degradation data in the first 12 hrs is shown in (c).

Sample ID	Type	f_G	f_P	f_S	W_G	W_P	W_S	Sample ID	Type	f_G	f_P	f_S	W_G	W_P	W_S
QL41	stream	0.20	0.73	0.08	0.48	0.46	0.02	QL67	spring	0.23	0.61	0.17	0.37	0.36	0.03
QL42	stream	0.26	0.68	0.06	0.35	0.34	0.02	QL71	spring	0.23	0.71	0.06	0.36	0.35	0.03
QL43	stream	0.31	0.65	0.04	0.49	0.47	0.02	QL72	spring	0.29	0.66	0.05	0.39	0.38	0.02
QL47	stream	0.26	0.68	0.06	0.42	0.41	0.02	QL88	spring	0.27	0.56	0.17	0.42	0.41	0.03
QL58	stream	0.22	0.73	0.05	0.38	0.36	0.02	QL104	spring	0.30	0.53	0.18	0.45	0.44	0.03
QL61	stream	0.24	0.73	0.04	0.40	0.38	0.02	QL1812	spring	0.22	0.61	0.17	0.36	0.35	0.03
QL64	stream	0.23	0.72	0.05	0.39	0.37	0.02	QL1813	spring	0.18	0.66	0.16	0.32	0.31	0.03
QL66	stream	0.24	0.66	0.10	0.39	0.38	0.02	QL1818	spring	0.23	0.58	0.19	0.37	0.36	0.03
QL68	stream	0.21	0.72	0.07	0.37	0.35	0.02	QL1819	spring	0.22	0.59	0.19	0.36	0.35	0.03
QL73	stream	0.23	0.59	0.18	0.37	0.36	0.03	QL1820	spring	0.21	0.61	0.18	0.35	0.34	0.03
QL83	stream	0.27	0.59	0.13	0.43	0.42	0.02	QL1821	spring	0.22	0.61	0.16	0.37	0.36	0.03
QL84	stream	0.25	0.64	0.11	0.40	0.39	0.02	QL1830	spring	0.31	0.64	0.05	0.48	0.46	0.02
QL85	stream	0.27	0.60	0.13	0.42	0.41	0.02	QL1831	spring	0.22	0.61	0.17	0.46	0.45	0.02
QL86	stream	0.26	0.61	0.13	0.42	0.40	0.02	QL65	groundwater	0.21	0.62	0.17	0.35	0.34	0.03
QL87	stream	0.22	0.62	0.16	0.36	0.35	0.02	QL94	groundwater	0.27	0.59	0.14	0.42	0.41	0.03
QL90	stream	0.30	0.54	0.16	0.47	0.45	0.03	QL95	groundwater	0.27	0.58	0.14	0.43	0.42	0.03
QL92	stream	0.29	0.55	0.16	0.44	0.43	0.03	QL98	groundwater	0.11	0.74	0.15	0.27	0.26	0.02
QL99	stream	0.26	0.66	0.08	0.42	0.40	0.02	QL1808	groundwater	0.17	0.66	0.17	0.31	0.31	0.03
QL100	stream	0.26	0.65	0.09	0.42	0.40	0.02	QL1809	groundwater	0.17	0.67	0.17	0.31	0.30	0.03
QL101	stream	0.25	0.66	0.09	0.41	0.40	0.02	QL1810	groundwater	0.21	0.59	0.20	0.34	0.33	0.03
QL102	stream	0.25	0.66	0.09	0.40	0.39	0.02	QL1811	groundwater	0.17	0.69	0.14	0.32	0.31	0.02
QL103	stream	0.25	0.66	0.09	0.40	0.39	0.02	QL1815	groundwater	0.20	0.60	0.20	0.34	0.33	0.03
QL106	stream	0.22	0.67	0.12	0.36	0.35	0.02	QL1840	groundwater	0.22	0.63	0.15	0.37	0.35	0.03
QL1814	stream	0.29	0.57	0.14	0.44	0.43	0.03	QL1841	groundwater	0.22	0.63	0.15	0.36	0.35	0.03
QL1816	stream	0.27	0.59	0.14	0.43	0.42	0.03	QL1842	groundwater	0.21	0.64	0.15	0.35	0.34	0.03
QL1817	stream	0.26	0.59	0.15	0.42	0.40	0.03								
QL1829	stream	0.29	0.66	0.05	0.46	0.44	0.02								
QL1832	stream	0.32	0.61	0.08	0.49	0.47	0.02								
QL1833	stream	0.31	0.61	0.08	0.48	0.46	0.02								
QL1834	stream	0.25	0.60	0.15	0.40	0.39	0.03								
QL1836	stream	0.45	0.50	0.04	0.68	0.66	0.03								
QL1837	stream	0.38	0.50	0.12	0.58	0.56	0.03								
QL1838	stream	0.23	0.68	0.09	0.38	0.37	0.02								
QL1839	stream	0.35	0.50	0.15	0.54	0.52	0.03								
QL1844	stream	0.50	0.46	0.04	0.75	0.72	0.03								

Table S1. Unmixed fractions of glacier-snow (f_G), precipitation (f_P) and soil (f_S) endmember contributions and the associated uncertainties for glacier-snow (W_G), precipitation (W_P) and soil (W_S). For isotopic and EC "conservative" tracer concentrations and other chemical data of each sample, see Dataset S1 and S2.

Depth b.s.l	Time (d)	DOC (mg/ L solution)	DOC (mg/g wet soil)	$SUVA_{254}$ (L mg $C^{-1}m^{-1}$)	Protein-like percent	FI	BIX	Protein-like intensity (RU)
profile 1: thawed soil in seasonal permafrost zone near red mud gully (38.2630N, 99.8777E, 2850 m a.s.l)								
5 cm	3	13.1	0.05	3.48		1.33	0.48	
	40	282.8	1.10	0.88		1.41	0.47	
15 cm	3	10.0	0.04	3.53	22%	1.29	0.52	0.12
	40	125.4	0.35	0.98	11%	1.53	0.52	0.10
30 cm	3	13.6	0.02	3.79	29%	1.38	0.60	0.25
	40	16.1		3.87	13%	1.50	0.52	0.12
50 cm	3	27.8	0.05	1.71	42%	1.54	0.69	0.45
	40	33.1	0.06	1.88	13%	1.50	0.52	0.12
profile 2: dried thermokarst sediment (38.2423N, 99.8859 E, 3500 m a.s.l)								
10 cm	3	15.4	0.24	4.07	22%	1.33	0.53	0.22
	40	34.4	0.13	6.13	7%	1.41	0.48	0.17
30 cm	3	15.6	0.03	2.92	33%	1.51	0.60	0.34
	40	23.6	0.05	4.27	19%	1.43	0.54	0.13
80 cm	3	16.6	0.03	2.83	33%	1.47	0.58	0.39
	40	34.0	0.05	2.98	22%	1.35	0.53	0.18
profile 3: wet thermokarst sediment (38.2443N, 99.8879 E, 3500 m a.s.l)								
10 cm	1	18.7	0.06	1.48	20%	1.43	0.48	0.13
	3	44.8	0.14	1.33	10%	1.38	0.46	0.05
	40	46.8	0.16	4.18	6%	1.42	0.49	0.07
20 cm	1	28.0	0.07	2.08	19%	1.43	0.50	0.17
	3	53.3	0.14	1.93	9%	1.31	0.44	0.06
	40	42.5	0.12	4.40	9%	1.34	0.50	0.10
30 cm	1	23.1	0.06	2.51	19%	1.45	0.49	0.20
	3	63.5	0.16	1.80	9%	1.41	0.50	0.09
	40	38.9	0.11	4.44	7%	1.36	0.47	0.10
profile 4: permafrost zone (38.2414N, 99.8862E, elevation: 3600 m)								
5 cm	1	12.4	0.09	3.64	18%	1.29	0.42	0.11
	3	24.4	0.20	2.91	61%	1.35	0.48	1.17
	40	129.5	0.80	1.29	40%	1.45	0.55	0.58
15 cm	1	13.4	0.06	3.80	17%	1.30	0.42	0.11
	3	15.3	0.06	4.45	15%	1.29	0.48	0.14
	40	55.4	0.27	2.42	13%	1.40	0.50	0.11
25 cm	1	15.8	0.08	2.92	21%	1.27	0.43	0.13
	3	18.0	0.09	3.20	13%	1.30	0.45	0.11
	40	99.2	0.57	1.64	20%	1.38	0.55	0.21
35 cm	1	11.6	0.05	5.05	20%	1.32	0.43	0.15
	3	18.9	0.07	4.30	19%	1.27	0.48	0.20
	40	32.5	0.11	3.38	23%	1.38	0.56	0.15

Table S2. DOC concentrations and fluorescence properties for four soil profiles in soil batch incubation experiment after 1, 3 and 40 extraction days.

Dataset S1. Detailed sampling information including water types, sampling date (year/month/date), locations (Lat., Long, and Elev.), electrical conductivity (EC, μS/cm). Calculations including proportions of glacier-snow meltwater, precipitation, and frozen soil meltwater end members (G, P, S) based on stable isotopes and EC, the expected initial DOC (DOC_0) and utilized DOC (ΔDOC). DOC concentrations (mg L^{-1}) and DOM optical parameters including $SUVA_{254}$ (L mg $C^{-1}m^{-1}$), fluorescence index (FI), freshness index (BIX), percentage proportions of protein-like component (%) derived from PARAFAC.

* Only DOC concentrations were available for samples collected in Apr 2012. One thermokarst sample collected near the west tributary was excluded in the data analysis.

‡ The 7 groundwater samples were collected from the same monitoring well screened at 30 m at the outlet (see MW in Fig.1d and Fig 3).

† The four groundwater samples were collected from the WW3 well (see WW3 in Fig.1d) located in piedmont sloping plain dominated by seasonal frost, with screened intervals being 5, 10, 20 and 30 m underground, respectively.

§ The groundwater/well water was collected from the WW4 with depth at 1m without pumping.

† The groundwater sample was collected from the WW1 well screened at 25 m (WW1 in Fig.1d).

Dataset S2. Additional field measurements including water temperature, pH, alkalinity (Alk, meq L^{-1}), dissolved oxygen (DO, mg L^{-1}). Concentrations of major ions and total nitrogen (TN, mg L^{-1}). The intensity loadings of the four components derived from PARAFAC (C1 to C4).

Reference

Catala, T. S., et al. (2015), Turnover time of fluorescent dissolved organic matter in the dark global ocean, *Nature Communications*, *6*.

D'Andrilli, J., J. R. Junker, H. J. Smith, E. A. Scholl, and C. M. Foreman (2019), DOM composition alters ecosystem function during microbial processing of isolated sources, *Biogeochemistry*, *142*(2), 281-298.

Gran, G. (1952), Determination of the equivalence point in potentiometric titrations. Part II, *Analyst*, *77*(920), 661-671.

Murphy, K. R., C. A. Stedmon, D. T. Waite, and G. M. Ruiz (2008), Distinguishing between terrestrial and autochthonous organic matter sources in marine environments using fluorescence spectroscopy, *Marine Chemistry*, *108*(1-2), 40-58.